LOW TEMPERATURE SCANNING TUNNELING MICROSCOPE AND ITS APPLICATION TO MATERIAL CHARACTERIZATION

A Thesis

by

MINJIE LU

Submitted to the Office of Graduate and Professional Studies of
Texas A&M University
in partial fulfillment of the requirements for the degree of

DOCTOR OF PHILOSOPHY

Chair of Committee,	Glenn Agnolet
Co-Chair of Committee,	Donald G. Naugle
Committee Members,	Wayne M. Saslow
	Tahir Cagin
Head of Department,	Grigory V. Rogachev

August 2020

Major Subject: Physics

ABSTRACT

A low temperature and high vacuum compatible fiber optic interferometer was designed and constructed to debug a malfunctioning low temperature scanning tunneling microscope (LT-STM). With its help, the temperature dependent behavior of a Pan-style piezoelectric actuator was studied. The scanning tunneling microscope (STM) was modified accordingly and worked reliably below 10 K.

Other properties of the STM were also improved. The electronic noise was reduced from hundreds of picoamps to approximately 10 picoamps by improving the shielding and avoiding ground loops. An eddy current damper was implemented to reduce the vibrational noise. A new mechanical sample stage was introduced to allow manipulation of the sample during experiments. As a result, beautiful atomic resolution images of graphite and self-assembled dodecanethiol monolayer on gold were obtained.

Scanning tunneling spectroscopy (STS) measurements were carried out on flux-grown HfNiSn single crystals. Instead of a semiconductor gap, a $V^{1/2}$ zero bias anomaly (ZBA) which typically presents in disordered systems was observed. Both the temperature dependent resistivity and the magnetoresistance of HfNiSn show characteristic features of disordered systems as well. Below 200 K, the resistivity saturates or obeys a 3 dimensional variable-range hopping (VRH) behavior. The magnetoresistance can be well explained by the Fukuyama-Hoshino (F-H) model for 3D weak anti-localization (WAL). These results indicate that the intrinsic anti-site disorder in HfNiSn may cause Anderson localization. In addition, theories developed and refined in the 1980's for the electron-electron interaction in disordered systems can be used to understand the physical properties and to guide the modifications of half Heusler materials.

ACKNOWLEDGMENTS

First, thanks for Dr. Glenn Agnolet's continuous support during my PhD life. Thank you for hiring me as a research assistant for several years so that I could concentrate on research. Dr. Agnolet patiently taught me all about low temperature technology, the design of laboratory equipment, thermodynamics and much more. Especially, under the influence of Dr. Agnolet, I developed the habit of systematic analysis and planing ahead. These are essential characterisstics for not only performing successful experiments but also overcoming any challenge in life. Dr. Agnolet also generously allowed me to finish a masters degree in computer science which provides me a more flexible choice of career. I would like to thank all my committee members. I was able to get any academic assistance whenever I asked.

My mother, Nianhua Yan and my father, Liancai Lu, never imposed their views on me and always supported me to pursue my interest.

Garrick Garza and John Newkirk of the machine shop provided me countless guidance when I was machining the units which made the experiments possible. Steve Payne, Jason Caswell and James Kirby of the electronic shop fixed all the broken instruments. Especially, Jason made the control box for coarse approach which has been well-functioning for five years. Mark Platt of Dr. Rupak Mahapatra's group is an all-round technician. It is possible to get a solution for any tricky technical problem from him. Daya Rathnayaka also provided me countless technical advice. I also want to thank Dr. Lucia Steinke for providing me the HfNiSn single crystal.

Fedja Kadribasic, Hao Chen and all the undergraduate students together made life in the lab enjoyable. The list does not have an end.

CONTRIBUTORS AND FUNDING SOURCES

Contributors

This work was supported by a dissertation committee consisting of Professors Glenn Agnolet [advisor], Donald G. Naugle [co-advisor] and Wayne M. Saslow of the Department of Physics & Astronomy and Professor Tahir Cagin of the Department of Materials Science and Engineering.

The HfNiSn single crystal which is the main topic of Section 3 was provided by Dr. Lucia Steinke. The temperature dependent resistivity and the magnetoresistance of HfNiSn depicted in Fig. 3.1, 3.2, 3.8 and 3.9 were also provided by her and were used in an article [1] uploaded to arXiv. The three samples of ZrNiPb, ZrCoSb and NbFeSb mentioned in Section 3 was provided by Fei Tian of Dr. Zhifeng Ren's group of the University of Houston.

All other work conducted for the thesis (or) dissertation was completed by the student independently.

Funding Sources

Graduate study was supported by a fellowship from Texas A&M University and a dissertation research fellowship from the Nelson M. Duller Endowment Fund.

NOMENCLATURE

LT-STM	Low Temperature Scanning Tunneling Microscope
LDOS	Local Density of States
STS	Scanning Tunneling Spectroscopy
ZBA	Zero Bias Anomaly
VRH	Variable-Range Hopping
WAL	Weak Anti-Localization
UHV	Ultra High Vacuum
IETS	Inelastic Scanning Tunneling Spectroscopy
LIA	Lock-In Amplifier
OFHC	Oxygen-Free High Thermal Conductivity Copper
FCC	Face-Centered Cubic Space Group
XRD	X-Ray Diffraction
EMPA	Electron Micro Probe Analyzer
DFT	Density Functional Theory
IR	Infrared Light
ZT	The Thermoelectric Figure of Merit
NNH	Nearest Neighbor Hopping
SEM	Scanning Electron Microscope
TLS	Two Level System
CI	Coulomb Interaction

TABLE OF CONTENTS

Page

LIST OF FIGURES

LIST OF TABLES

TABLE Page

1. INTRODUCTION AND LITERATURE REVIEW

1.1 Low Temperature Technologies

Many interesting physics phenomena manifest at low temperatures (LT) when the relevant energy scale for the phenomena such as the coupling energy becomes large compared to the energy scale of thermal fluctuations which is proportional to $k_B T$. Superconductivity which is characterized by zero resistance and the complete expulsion of an external magnetic field was discovered by Kamerlingh Onnes in mercury at 4.2 K because he was the first person to liquify ^{4}He. ^{4}He has a boiling point of 4.2 K under 1 atmosphere which is the second lowest among all gases. Bose-Einstein condensation is a state of a system of bosons in which a large fraction of the bosons settle in the lowest energy state. This phenomenon was predicted by Satyendra Bose and Albert Einstein, and verified experimentally by Eric Cornell and Carl Wieman. In their experiment, diluted rubidium-87 gas was cooled to 170 nK, very close to absolute zero which is not reachable according to the third law of thermodynamics.

1.1.1 Dilution Refrigerator

One standard technique to cool down large material samples is the dilution refrigerator (DR). It was invented by Heinz London in 1951. The lowest temperature achieved by a dilution refrigerator is 1.75 mK. The key component of a DR is the mixing chamber. When a refrigerator is operating, there will be two phases of ^{3}He and ^{4}He inside the mixing chamber. One is concentrated ^{3}He and the other is a dilute ^{3}He-^{4}He mixture. ^{3}He passing through the boundary from the concentrated phase to the dilute phase constitues an endothermic process. Figure 1.1 shows the phase diagram for the ^{3}He and ^{4}He mixture at LT and Fig. 1.2 shows the structure of a dilution refrigerator.

In continuous operation ^{3}He circulates through the DR. ^{3}He gas of a few hundreds of millibars is precooled by liquid nitrogen to 77 K and by liquid ^{4}He to 4.2 K. Afterwards, it is further cooled by the 1K pot. The 1K pot temperature is achieved by constantly pumping liquid ^{4}He using a powerful mechanical pump to lower its boiling point. Before entering the mixing chamber, the

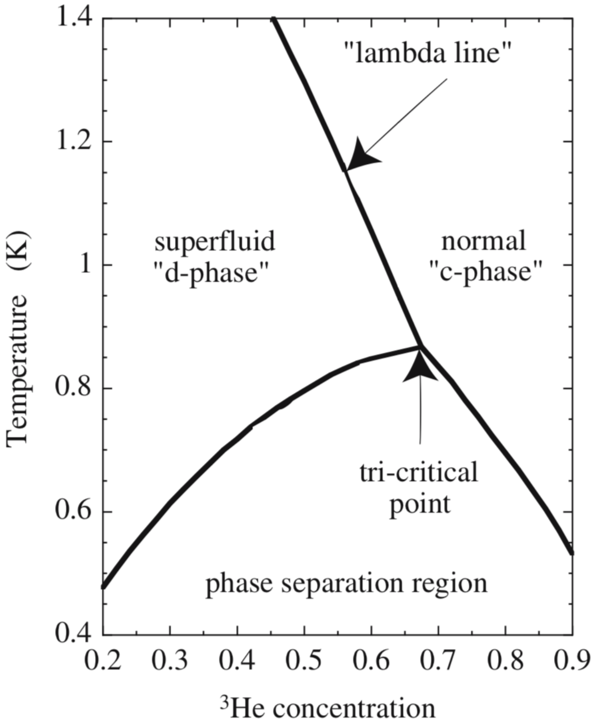

Figure 1.1: Phase diagram of ^{3}He and ^{4}He mixture. "d-phase" stands for the ^{3}He dilute phase. "c-phase" stands for the ^{3}He concentrated phase. Reprinted from [2] with permission.

^{3}He must be precooled as much as possible. Therefore, while it is impeded in a very narrow capillary, it exchanges heat with the still that operates from 500 mK to 700 mK. Subsequently, at several more stages the incoming ^{3}He exchanges heat with the outgoing colder ^{3}He coming from the mixing chamber. The still is pumped by a powerful roots blower and a mechanical pump to form the circulation of ^{3}He. According to the phase diagram of the ^{3}He and ^{4}He mixture, the vapor of the mixture at a temperature of less than 1K should be mainly be comprised of ^{3}He. Therefore, primarily only ^{3}He is pumped from the still.

The cooling power of a dilution refrigerator is given by

$$\dot{Q}_m = \dot{n}_3(95T_m^2 - 11T_i^2) \tag{1.1}$$

where $\dot{n}_3$ is the molar circulating rate of ^{3}He. T_m is the temperature of the mixing chamber and T_i is

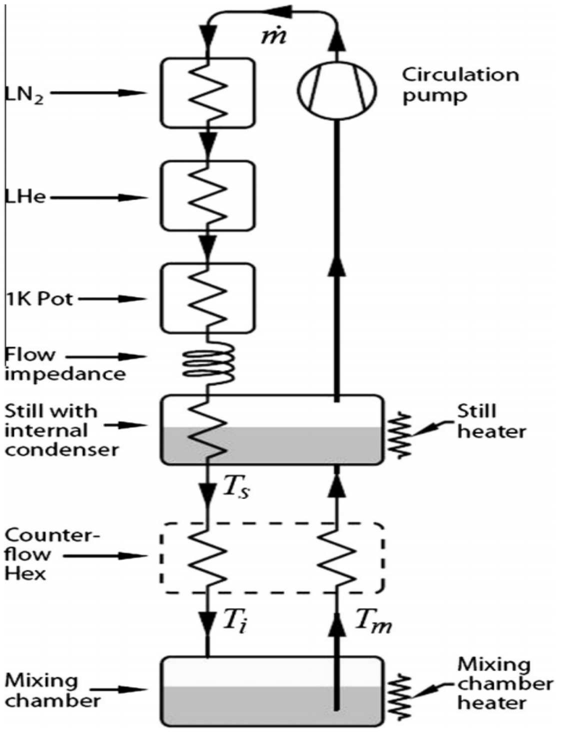

Figure 1.2: An illustration of the main components of a dilution refrigerator. Reprinted from [3] with permission.

the temperature of the ^{3}He liquid entering the mixing chamber. When the system is at equilibrium and there is no heat load, setting $\dot{Q}_m$ to zero, we obtain $T_m = \frac{T_i}{2.8}$. Therefore, for a fixed ^{3}He circulating rate, lowering T_i allows us to reach a lower base temperature.

Nowadays, instead of using a combination of liquid nitrogen, ^{4}He and 1K pot to precool ^{3}He, a cryocooler such as a pulse tube cooler is used to liquify the incoming ^{3}He. Fridges using these two kinds of techniques are called wet and dry fridges. Even though a dry fridge saves cryogens and can provide potentially lower base temperatures than a wet one, the pulse tube is major source of mechanical vibrations. It therefore takes more effort to carry out vibration sensitive experiments in these fridges as a customized vibration isolation and damping system should be designed.

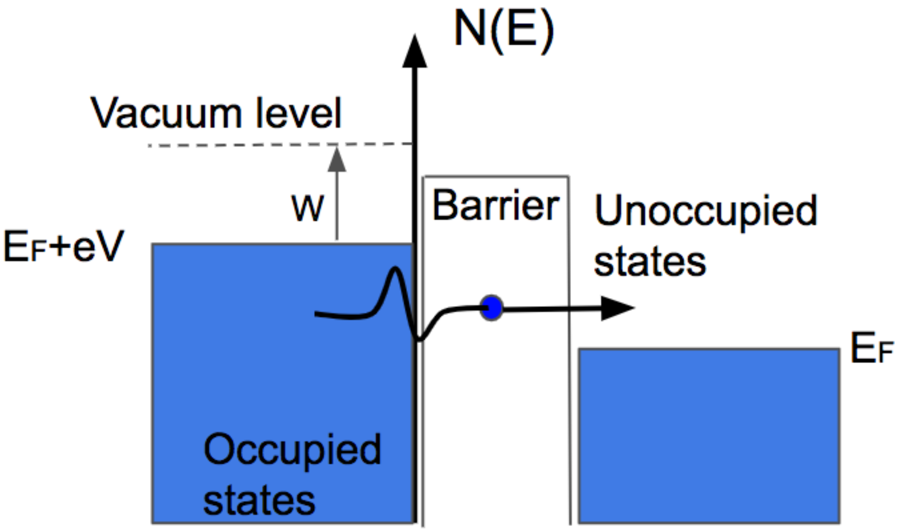

Figure 1.3: An illustration of electron tunneling. E_F is the Fermi level of the tip. W is the work function of the sample. V is the voltage drop across the tunneling junction.

1.2 Scanning Tunneling Microscopy

1.2.1 Bardeen's Model for the Tunneling Current

Bardeen implements a time dependent perturbation theory to explain the current in tunneling experiments [22] (see Fig. 1.3). We start from separate Schrodinger equations for the sample and the tip.

$$(-\frac{\hbar^2}{2m}\frac{\partial^2}{\partial z^2}+U_i)\psi^i = i\hbar\frac{\partial\psi^i}{\partial t} \tag{1.2}$$

where i stands either for the sample (S) or the tip (T). Assuming stationary states, $\psi^i = \psi^i_\mu e^{-iE^i_\mu t/\hbar}$, the stationary Schrodinger equations becomes

$$(-\frac{\hbar^2}{2m}\frac{\partial^2}{\partial z^2}+U_i)\psi^i_\mu = E^i_\mu\psi^i_\mu \tag{1.3}$$

The entire tunneling process can be treated adiabatically because the time scale for electrons to tunnel is femtoseconds whereas the time scale to mechanically move the tip is seconds. Initially at $t=-\infty$, the tip is far away from the sample and the electrons in the sample only see the sample potential, U_s. As the tip approaches, an increasing contibution of the tip potential is added. This potential can be modeled as $U_T(t) = e^{\eta t/\hbar}U_T$, resulting in

$$(-\frac{\hbar^2}{2m}\frac{\partial^2}{\partial z^2} + U_S + e^{\eta t/\hbar}U_T)\psi = i\hbar\frac{\partial\psi}{\partial t} \tag{1.4}$$

where η is a small and positive coefficient. When there is no more relative motion between the sample and the tip, we can take $t \to 0$, resulting in the final configuration of a combined potential, $U_\mathrm{S} + U_\mathrm{T}$. Therefore, during the process, an initial state in the sample will evolve to

$$\psi = a_\mu[t]\psi_\mu^S e^{-iE_\mu^S t/\hbar} + \sum_{\nu=1}^{\infty} c_\nu[t]\psi_\nu^T e^{-iE_\nu^T t/\hbar} \tag{1.5}$$

Plugging Eqs. 1.3 and 1.5 into Eq. 1.4, we obtain

$$\begin{aligned} &a_\mu[t]U_T\psi_\mu^S e^{(\eta - iE_\mu^S)t/\hbar} + \sum_{\nu=1}^{\infty} c_\nu[t]\psi_\nu^T e^{-iE_\nu^T t/\hbar} \\ &= i\hbar\psi_\mu^S e^{-iE_\mu^S t/\hbar}\frac{da_\mu[t]}{dt} + i\hbar\sum_{\nu=1}^{\infty}\psi_\nu^T e^{-iE_\nu^T t/\hbar}\frac{dc_\nu[t]}{dt} \end{aligned} \tag{1.6}$$

Projecting onto a stationary state ψ_ν^T gives us the tunneling amplitude from the initial state of the sample, ψ_μ^S, to a state ψ_ν^T of the tip. To simplify the equation, we make three assumptions: (1) states of the tip and the sample are approximately orthogonal, meaning $\int \psi_\mu^T \psi_\nu^S d^3r \approx 0$, (2) $a_\mu[t]$ evolves slowly, leading to $\frac{da_\mu[t]}{dt} = 0$ and (3) only constant terms are kept. Terms containing $c_\nu[t]$ are second-order infinitesimal quantities. As a result, we get a simple equation

$$i\hbar\frac{dc_\nu[t]}{dt} =< \psi_\nu^T|U_T|\psi_\mu^S > e^{-i(E_\mu^S - E_\nu^T + i\eta)t/\hbar} \tag{1.7}$$

Here, the amplitude of the initial state $a_\mu[t]$ remains approximately equal to 1 during this process.

Integrating with respect to t from $-\infty$ to t and taking the absolute square of $c_\nu(t)$, we can obtain the tunneling probability, $P_{\mu\nu}[t]$.

$$P_{\mu\nu}[t] = |c_\nu[t]|^2 = \frac{e^{2\eta t/\hbar}}{(E_\mu^S - E_\nu^T)^2 + \eta^2} | < \psi_\nu^T | U_T | \psi_\mu^S > |^2 \tag{1.8}$$

The derivative of the probability is the transition rate, $W_{\mu\nu}[t] = \frac{dP_{\mu\nu}[t]}{dt}$,

$$W_{\mu\nu}[t] = \frac{2\eta}{(E_\mu^S - E_\nu^T)^2 + \eta^2} e^{2\eta t/\hbar} \frac{1}{\hbar} |M_{\mu\nu}|^2 \tag{1.9}$$

where $M_{\mu\nu} = < \psi_\nu^T | U_T | \psi_\mu^S >$ is called the tunneling matrix.

As was mentioned previously, when the tip stops, one can take $t = 0$. In addition, one can take the limit as $\eta \to 0$. In this limit, $\lim_{\eta \to 0} \frac{\eta}{(E_\mu^S - E_\nu^T)^2 + \eta^2} \to \pi \delta[E_\mu^S - E_\nu^T]$ so that

$$W_{\mu\nu}[t] = \frac{2\pi}{\hbar} \delta[E_\mu^S - E_\nu^T] |M_{\mu\nu}|^2 \tag{1.10}$$

Due to the Pauli exclusion principle, electrons can only tunnel from an occupied state to an unoccupied state. The occupancy of a state is given by the Fermi distribution function, $f[E - E_F] = \frac{1}{1 + e^{(E - E_F)/k_B T}}$. When a bias voltage V is applied to the sample, the tunneling current from the sample to the tip I_{ST} and vice versa I_{TS} can be obtained by summing over all possible state pairs.

$$\begin{aligned} I_{ST} &= \frac{4\pi e}{\hbar} \sum_{\nu\mu} f[E_\mu^S - E_F^S](1 - f[E_\nu^T - E_F^T]) |M_{\mu\nu}|^2 \delta[E_\nu^T - E_\mu^S - eV] \\ I_{TS} &= \frac{4\pi e}{\hbar} \sum_{\nu\mu} f[E_\mu^T - E_F^T](1 - f[E_\nu^S - E_F^S]) |M_{\mu\nu}|^2 \delta[E_\nu^T - E_\mu^S - eV] \end{aligned} \tag{1.11}$$

where the factor of two takes into account the two possible values of the spin of the electrons.

Therefore, the net current from the sample to the tip is

$$I = I_{ST} - I_{TS} = \frac{4\pi e}{\hbar} \sum_{\nu\mu} (f[E_\mu^S - E_F^S] - f[E_\nu^T - E_F^T]) |M_{\mu\nu}|^2 \delta[E_\nu^T - E_\mu^S - eV] \tag{1.12}$$

Because a real crystal has a macroscopic volume, the electronic states are continuous rather than discrete. Suppose that the density of states for the sample and the tip are given by $n^S[E^S]$ and

$n^T[E^T]$ respectively. The total tunneling current then becomes

$$\begin{aligned} I =& \frac{4\pi e}{\hbar} \int d\epsilon \, (f[E_F^T - eV + \epsilon] - f[E_F^S + \epsilon]) \\ & \times n^T[E_F^T - eV + \epsilon] n^S[E_F^S + \epsilon] |M[E_F^T - eV + \epsilon, E_F^S + \epsilon]|^2 \end{aligned} \tag{1.13}$$

We can further simplify this expression by assuming that the density of states of the tip is approximately a constant around the Fermi energy and that the Fermi distribution functions can be approximated by Heaviside step functions at sufficiently low temperatures.

$$I = \frac{4\pi e}{\hbar} \int_0^{eV} d\epsilon \, n^T[E_F^T - eV + \epsilon] n^S[E_F^S + \epsilon] |M[E_F^T - eV + \epsilon, E_F^S + \epsilon]|^2. \tag{1.14}$$

Taking the derivative of the tunneling current with respect to the bias voltage V, we obtain

$$\frac{dI}{dV} = \frac{4\pi e}{\hbar} n^T[E_F^T] n^S[E_F^S + eV] |M[E_F^S + eV, E_F^T]|^2 \tag{1.15}$$

This shows that an STM can measure the density of states $n^S[\epsilon] = \int d\vec{k} \delta[\epsilon - \epsilon_{\vec{k}}]$, or the local density of states $n^S[\epsilon] = \int d\vec{k} \delta[\epsilon - \epsilon_{\vec{k}}] |\psi[\vec{k}, \vec{r}]|^2$ at the tip. One advantage of the STM is its ability to measure both the occupied and unoccupied states by simply reversing the bias voltage. Techniques like phonon absorption and angle resolved photon emission spectroscopy (ARPES) require stimulating electrons out of the material and therefore can only detect the occupied states.

1.2.2 Tersoff-Hamann Model

Bardeen's model contains a convolution between the density of states of the sample and the states of the tip, weighted by the tunneling matrix $M_{\mu\nu}$. To calculate $M_{\mu\nu}$, wave functions are needed. However it is generally very difficulty to determine these parameters for a general tip. To avoid this problem, the Tersoff-Hamann (TH) Model suggests that the tip can be approximated by a single atom with an s-orbital wave function.

$$\psi_\nu^T[\vec{r} - \vec{R}_T] = C\frac{e^{-\kappa|\vec{r}-\vec{R}_T|}}{\kappa|\vec{r} - \vec{R}_T|} \tag{1.16}$$

where $\vec{R}_T$ is the position of the tip and $\kappa = \sqrt{\frac{2mE}{\hbar^2}}$. Plugging this wavefunction into the formula for $M_{\mu\nu}$ and taking n^T as a constant, the tunneling current becomes

$$I[\vec{R}_T, V] = \frac{16\pi^3 C^2 \hbar^3 e}{\kappa^2 m^2} n^T \int_0^{eV} d\epsilon \int d\vec{k}\delta[\epsilon - \epsilon_{\vec{k}}]|\psi[\vec{k}, \vec{R}_T]|^2 \tag{1.17}$$

Then the conductance becomes

$$\frac{dI[\vec{R}_T, V]}{dV} = \frac{16\pi^3 C^2 \hbar^3 e}{\kappa^2 m^2} n^T \int d\vec{k}\delta[E_F^S + eV - \epsilon_{\vec{k}}]|\psi[\vec{k}, \vec{R}_T]|^2 \tag{1.18}$$

This equation provides an intuitive explanation as to why an STM measures the local density of states of the sample at $\vec{R}_T$.

Real experimental results are much more sophisticated than the situations described by the Bardeen and the TH model. But these models can still provide guidance for experiment design and the interpretation of results. Just as a wave function decays exponentially in a potential barrier, the wave functions of electrons in materials also decay exponentially from the surface. Therefore, the tunneling current is expected to decay exponentially with respect to the separation between the tip and the sample.

$$I \propto e^{-\alpha z} \tag{1.19}$$

1.3 STM Hardware

1.3.1 Coarse Approach

There are two important components of an STM. The first is the coarse approach unit. Because the tunneling current decays exponentially with the tip-sample distance, the STM can only operate with a tip-sample separation that is less than a few angstroms. A piezo tube can only retract or

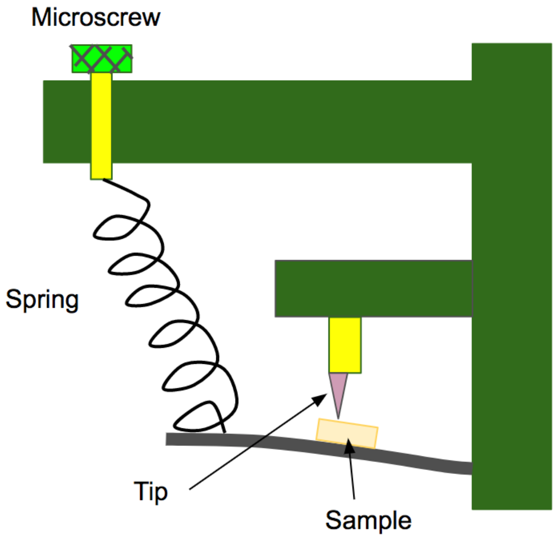

Figure 1.4: A mechanical positioner for STM.

extend the tip by a few hundreds of nanometers. In order to bring the tip precisely hundreds of nanometers away from the sample surface, a mechanism called the coarse approach is needed. I will introduce some typical coarse approach designs here.

A **mechanical positioner** is easy to implement because it doesn't involve piezoelectric materials or any complex control electronics. One possible design is to use a combination of a micro screw and a spring as shown in Fig. 1.4.

The micro screw transfers a visible rotational displacement to a small imperceptible linear displacement stretching the spring. It forms a serial spring system with the metal plate on which the sample sits that further distributes the deformation. With a proper choice of the pitch of the screw and the elastic coefficients of the spring and the metal plate, one can achieve a fine control of hundreds of nanometers movement. However, this simple design has disadvantages including poor mechanical stability and nonuniform step sizes.

A **louse positioner** [5] has three feet at each corner of a triangular piezo plate. Each foot can be fixed by a magnetic field generated by magnetic coils. The tip attached to the piezo plate can then be moved by the following procedure: (1) shrink the piezo plate while one foot is free and the other two feet are fixed, (2) fix the foot that was free and release the feet that were fixed and (3)

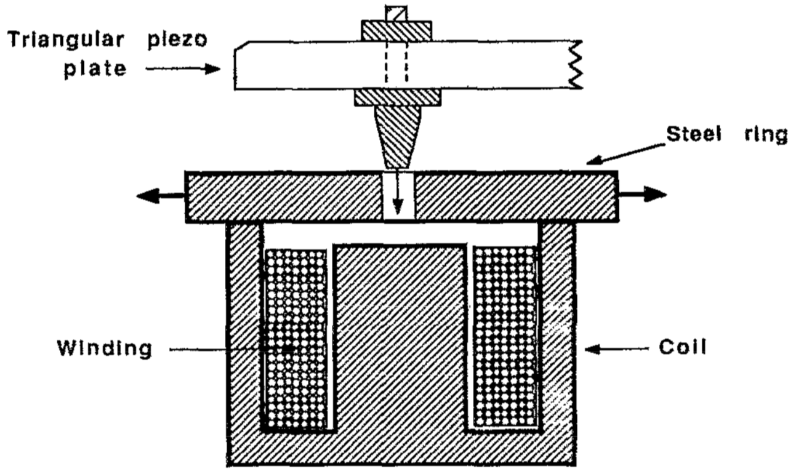

Figure 1.5: One of the three feet of a Louse positioner. Reprinted from [5] with permission.

stretch the piezo plate. Fig. 1.5 shows the configuration of one foot.

A louse positioner was the first piezo based coarse approach mechanism that was successfully functional for STM. A single step can range from 10 nm to $1\,\mu\mathrm{m}$. With more complex controls, the tip is free to move within the entire 2 dimensional plane defined by the piezo plate. However, because the louse positioner does not have the rotational symmetry around the tip, it is not a good choice for low temperature applications. The beetle positioner and the Pan-style positioner are better candidates for low temperature STMs.

A **beetle positioner** is shown in Fig. 1.6. Four piezo tubes are attached to a round plate. They all have four electrodes and are capable of bending in both the x and y directions. The central tube is responsible for scanning and has the tip hanging at its bottom. The other three tubes have sapphire balls attached at the bottom that sit on three ramps (Only two are shown in Fig. 1.6). By applying ramp voltages to these three tubes, the top plate can rotate azimuthally utilizing its inertia. Because these tubes have a constant natural length, settling on a different point on the ramp lowers or raises the top plate and thus the tip. By properly manipulating the three supporting tubes in other manners, the top plate and the tip can also be moved horizontally instead of vertically to study a large area across the sample surface. Because the four piezo tubes in the beetle-style positioner are identical, their thermal contraction coefficient and speeds of sound are the same. Therefore, the

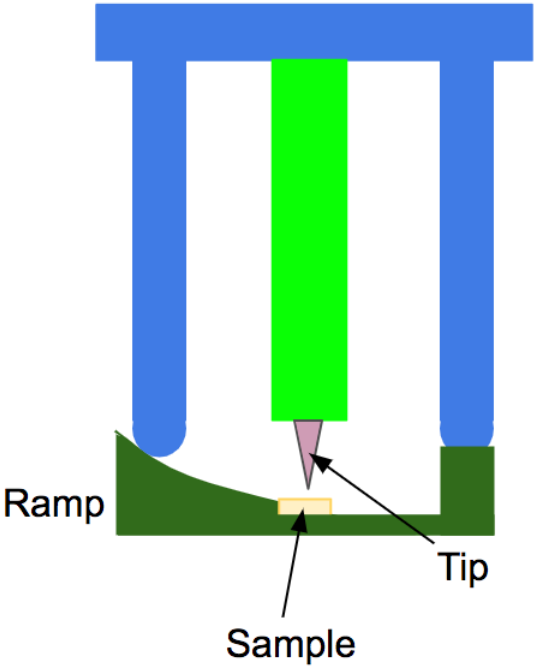

Figure 1.6: Design of a Beetle positioner.

Beetle positioner has good thermal and vibrational stability.

A **Pan-style positioner** was invented by Dr. Shuheng Pan in 1999 [14]. It is commonly used in low temperature STMs. Because it is also the coarse approach mechanism adopted by our lab, it will be introduced in more detail later.

1.3.2 Scanner

After a tunneling current is detected, the scanner moves the tip and scans the sample surface to obtain images. There are three kinds of common scanners.

A **tripod scanner** was used in many of the earlier STM's. As illustrated in Fig. 1.7, motions in x, y and z directions are actuated by three piezo pillars separately. Some of the disadvantages of this design are: (1) it is hard to combine it with a coarse positioner to quickly approach the tip to the sample, (2) the configuration is very asymmetric leading to poor stability under thermal contraction and (3) it is very difficult to calculate its resonance frequency making it difficult to reduce vibrational noise.

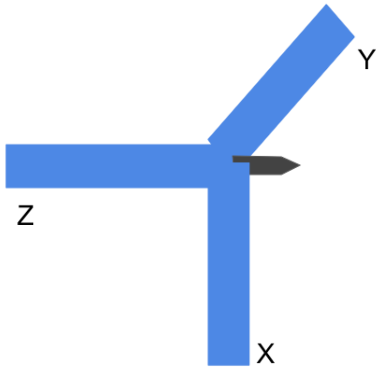

Figure 1.7: A tripod scanner. Three blue rods are piezo pillars in orthogonal xyz directions.

A **bimorph scanner** is comprised of two piezo plates glued together. Figure 1.8 shows the two common configurations of the bimorph scanner. The upper sketch of Fig. 1.8 is the parallel bimorph. Both exposed surfaces of the piezo plates are grounded. Voltage is applied to the interface between the two plates. Because the two plates are poled in the same direction, a voltage will cause one of the plate to shrink and the other to extend resulting in a bending motion. The lower sketch shows the serial bimorph configuration which applies a uniform electric field through two plates that are oppositely poled. One advantage of the parallel mode over the serial mode is that the stray fields are shielded. Therefore, it induces less electronic noise. However, both modes are hard to be assembled into a three dimensional scanner.

A **tube scanner** is shown in Fig. 1.9. This is the most commonly used scanner in modern STMs. Five electrodes are electroplated onto a piezoelectric tube. A z electrode covering the entire inner surface controls the vertical contraction and expansion when a voltage V_z is applied . On the outer surface, two x electrodes are opposite to each other and the same for the two y electrodes. Each of them cover a quarter of the outer perimeter. During scanning, bipolar voltages $+V_x$, $-V_x$ and $+V_y$, $-V_y$ are applied to the two x and two y electrodes simultaneously. This design substantially reduces the nonlinearity and interference of motions in different directions. Further improvement can be made by designing a more sophisticated control system.

Figure 1.10 shows another popular configuration of concentric tubes. The outer tube can be

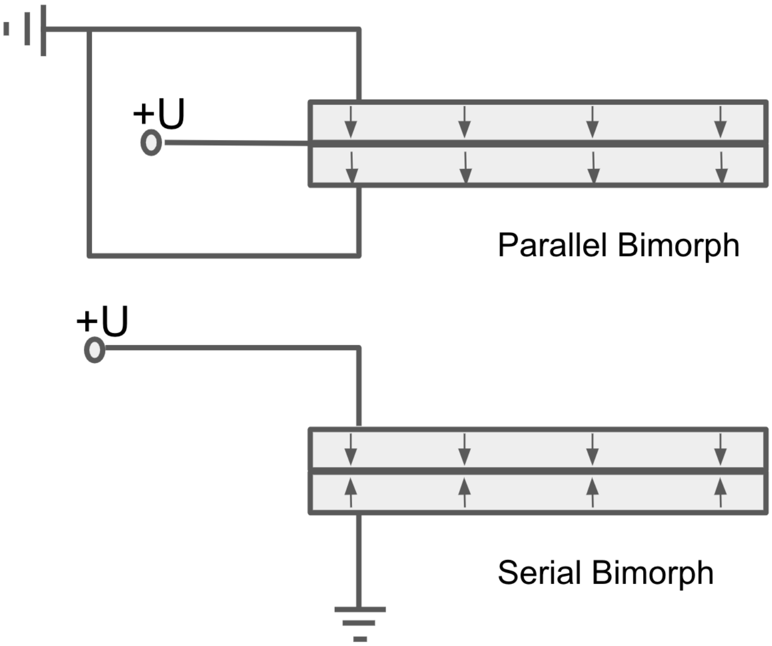

Figure 1.8: Parallel and serial Bimorph scanner. Arrows indicate the poling directions of piezo plates.

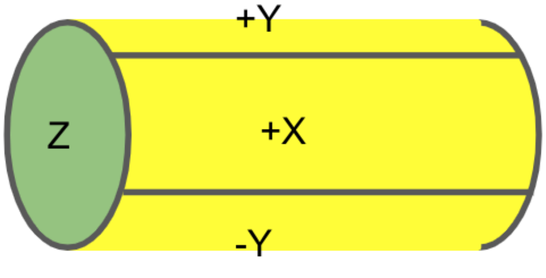

Figure 1.9: A tube scanner. The -X electrode sits opposite to the +X electrode. It can not be seen in this image.

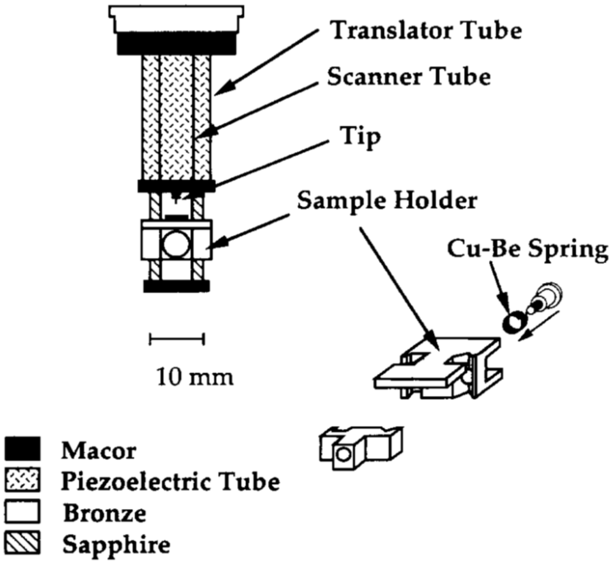

Figure 1.10: A concentric tube scanner. The tip is fixed on the inner scanner tube and the sample stage is fixed on the outer translator tube. Reprinted from [6] with permission.

used as a coarse positioner in both x, y and z directions allowing a larger scan area. But this design is usually subject to a larger drift.

1.4 Examples of STM Experiments

1.4.1 Atomic Resolution Images

As described in the theory section, STM current is an integral of the sample's LDOS over energy and therefore represents the contour of electron density and therefore agrees with the crystal structure of the material.

It is easier to achieve atomic resolution images on layered or semiconductor materials. Layered materials allow convenient cleavage which is very necessary for surface sensitive technologies like STM. Therefore, highly oriented pyrolytic graphite is commonly used to initially test the functionality of a STM.

Figure 1.11 shows an image of HOPG acquired by our STM. During the scan, there is a sudden change of corrugation. This phenomenon supports the importance of the tip states in an STM experiment. When the tip states changes, a complete different pattern can appear. There is also

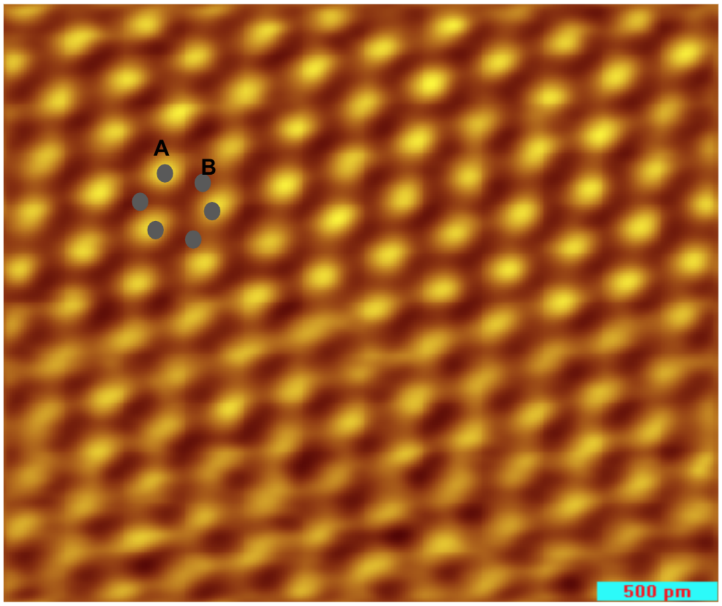

Figure 1.11: A 30 Å×30 Å image of HOPG produced by the LT-STM in our lab. Note the sudden change in the contrast that indicates that the configuration of the tip has changed. As expected only one half of the atoms are visible. The six dark gray points show the theoretical honeycomb structure.

possibility for corrugation inversion in which case protrusions turn into depressions and depressions turn into protrusions. Due to this reason, people are confused by the variety of different HOPG images published.

Unlike the expected honeycomb lattice, STM images of HOPG often show a triangular lattice with a lattice constant 2.46 Å. In this case, only one carbon atom in a unit cell appears. Other images may include two atoms but with different apparent heights. These results are explained by two aspects: (1) in I. P. Batra et al. [23] , the authors consider the influence of the second graphene layer beneath the surface. Because these two layers of graphene are interleaved as shown in Fig. 1.12, half of the carbon atoms (A atoms) on the surface have a neighbor in the underneath layer and the other half (B atoms) do not. Consequently, the wave function of the B atoms will be pulled down closer to the underneath layer causing a decrease in the LDOS on the surface, (2) by modeling the tip either as a trigonally symmetric plane of graphite, a dimer or a four atoms plane, R. J. Colton [24] is able to simulate most of the experimental results.

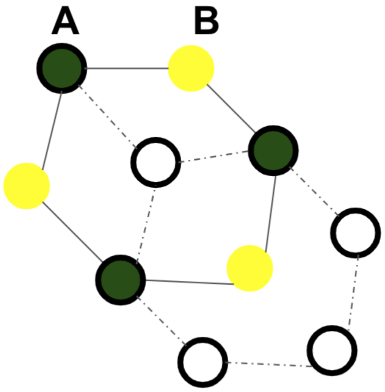

Figure 1.12: A sketch of the crystal structure of graphite. Solid circles connected by solid lines are the top layer. Open circles connected by dashed lines are the second layer. A atoms (green) have neighbors in the second layer. B atoms (yellow) do not.

Resolving atoms on a metallic surface is much harder than for surfaces of graphite or semiconductors. Because an STM detects the profile of the electron density around the Fermi level, the electronic wavefunctions in a semiconductor are more likely to be localized leading to a larger corrugation. However in metals, the electrons are mobile and their wavefunctions are approximately plane waves. As a result, the corrugation of semiconductor atoms can be at the level of an angstrom whereas it is only one tenth of an angstrom for metals. Another problem is that most metals can be easily oxidized. In order to obtain a fresh surface, sputtering and high temperature annealing should be integrated with the STM system in an ultra high vacuum (UHV) environment. In addition because the chemical bonds in semiconductors are localized, their surfaces usually go through reconstruction but this is generally not the case for metal. However, because gold undergoes a reconstruction into periodic strips the first atomic resolution image for metals was observed on the surface of inert gold (see Fig. 1.13).

Self assembly of molecular monolayers on metal is another interesting and important research field. It provides an approach to study heterogeneous catalysis, corrosion, adhesion and so on. In addition, some systems have the potential to become practical electronic devices. The mechanism by which current flows through a layer of molecules is more complex than other tunneling junctions

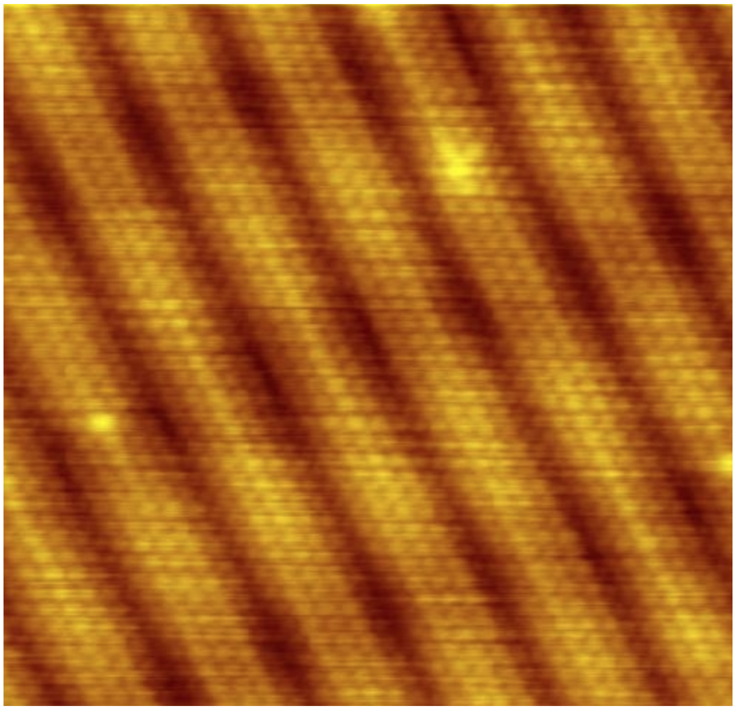

Figure 1.13: Periodic surface reconstruction on gold. Reprinted from [7]. Permission is not required for reprint.

and probably involves a mixture of hopping and tunneling mechanisms. In addition, the influence of vibrational modes and magnetic properties of the molecules can make the analysis even more complicated. For example, G. Doyen et al. [25] show that as the tip- sample separation decreases, the image of an absorbed oxygen atom on the surface of nickel will change from a bump to a hole.

1.4.2 Local Density of States

As indicated by the expression for the zero temperature current, Eq. 1.14,

$$I = \frac{4\pi e}{\hbar} \int_0^{eV} d\epsilon \, n^T[E_F^T - eV + \epsilon] n^S[E_F^S + \epsilon] |M[E_F^T - eV + \epsilon, E_F^S + \epsilon]|^2 \tag{1.20}$$

the tunneling current of the STM flows from occupied tip states to unoccupied sample states at positive bias, whereas at negative bias, the tunneling current flows from occupied sample states to unoccupied tip states. If we suppose that the Fermi level of the tip and the sample are the same when no bias is applied, then by taking $\epsilon = \epsilon + eV/2$, we can get a more symmetric form

$$I = \frac{4\pi e}{\hbar} \int_{-\frac{1}{2}eV}^{\frac{1}{2}eV} d\epsilon \;\; n^T[E_F - \frac{1}{2}eV + \epsilon] n^S[E_F + \frac{1}{2}eV + \epsilon)] |M[\epsilon]|^2 \tag{1.21}$$

The tunneling matrix here is not a constant.

$$M \propto e^{-\kappa s} \tag{1.22}$$

where s is the tip-sample separation. κ is given by

$$\kappa = \frac{\sqrt{2mE}}{\hbar} = \frac{\sqrt{2m(\bar{\phi} - \epsilon)}}{\hbar} \tag{1.23}$$

where E is the energy of the tunneling electron and $\bar{\phi}$ is the work function of electrons at $E_F + \frac{eV}{2}$. The relation between E, $\bar{\phi}$ and ϵ is clearly illustrated in Fig. 1.3.

In most cases, ϵ can be much smaller than $\bar{\phi}$ which allows an expansion of κ.

$$\kappa = \frac{\sqrt{2m\bar{\phi}}}{\hbar}(1 - \frac{\epsilon}{2\bar{\phi}}) = \kappa_0(1 - \frac{\epsilon}{2\bar{\phi}}) \tag{1.24}$$

Plugging Eq. 1.24 into Eq. 1.22, we obtain

$$M[\epsilon] = M[0] e^{\frac{\kappa_0 \epsilon s}{2\bar{\phi}}} \tag{1.25}$$

and therefore, Eq. 1.21 becomes

$$I = \frac{4\pi e}{\hbar} |M[0]|^2 \int_{-\frac{1}{2}eV}^{\frac{1}{2}eV} d\epsilon \, n^T[E_F - \frac{1}{2}eV + \epsilon] n^S[E_F + \frac{1}{2}eV + \epsilon] e^{\frac{\kappa_0 \epsilon s}{\bar{\phi}}} \tag{1.26}$$

In this way, if the tip-sample separation s and the bias voltage V are not too small, then for $V > 0$, most of the current comes from electrons tunneling from the states of the tip around the Fermi energy to the states of the sample around an energy of $E_F + eV$. The tunneling conductance

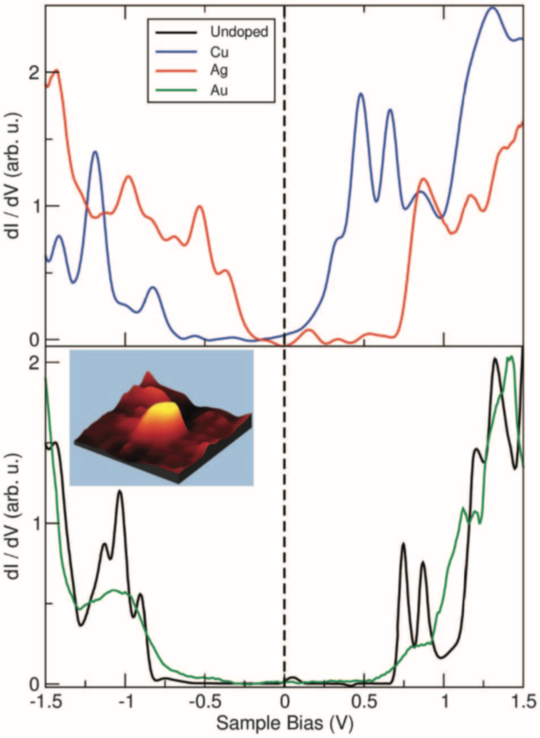

Figure 1.14: LDOS of undoped (black), Cu doped (Blue), Ag doped (Red) and Au doped (Green) InAs nanocrystals. Reprinted from [8] with permission.

is approximately

$$\frac{dI}{dV} \approx n^S[E_F + eV]n^T[E_F] \tag{1.27}$$

For $V < 0$, the situation is reversed and most of the current comes from electrons tunneling from the states of the sample around the Fermi energy to the states of the tip around an energy of $E_F + e|V|$

$$\frac{dI}{dV} \approx n^T[E_F + e|V|]n^S[E_F] \tag{1.28}$$

According to Eq. 1.27 and Eq. 1.28, at negative bias, we are detecting the DOS of the tip, whereas at positive bias, we are detecting the DOS of the sample. In practice, a large tip-sample separation is preferred to remove the influence of the convolution between the tip states and the sample states. However, a larger separation means a smaller signal and therefore a smaller signal to noise ratio. Therefore, a compromise should be made to determine the best separation.

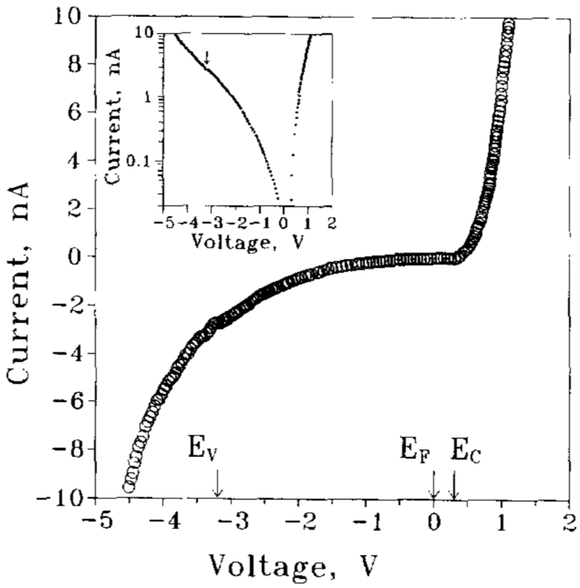

Figure 1.15: IV curve of a degenerate indium tin oxide film. The inset shows a semi-log graph. The arrow points to the inflection point corresponding to the edge of the valence band. Reprinted from [9] with permission.

LDOS delivers rich information about materials, from their categories to complex properties like the Landau levels in a magnetic field. Figure 1.14 shows LDOS of some colloidal semiconductor nanocrystals doped with metal atoms by D. Mocatta et al. [26]. A gap of 1.5 eV can be seen for the intrinsic material. When doped with different metal impurities, the gap width, the Fermi energy and the boundary of the valence and the conduction bands can all be modified. If the concentration of the impurity atoms becomes very high, impurity states can become continuous and finally fill the gap. In this case, the semiconductor becomes degenerate and starts to show metallic properties. However, the boundaries of the band gap can still be found by plotting the logarithmic LDOS versus the bias voltage. There will be two clear reflection points beyond which LDOS will grow with an increasing slope as shown in Fig. 1.15.

Another interesting physics phenomenon, Landau levels can also be studied by STM. P. Cheng [10] observed Landau levels in Bi_2Se_3 which is a well known topological insulator. Their LDOS result is shown in Fig. 1.16. Topological insulators have surface states that have time reversal symmetry and consequently backscattering by nonmagnetic impurities is forbidden. Therefore,

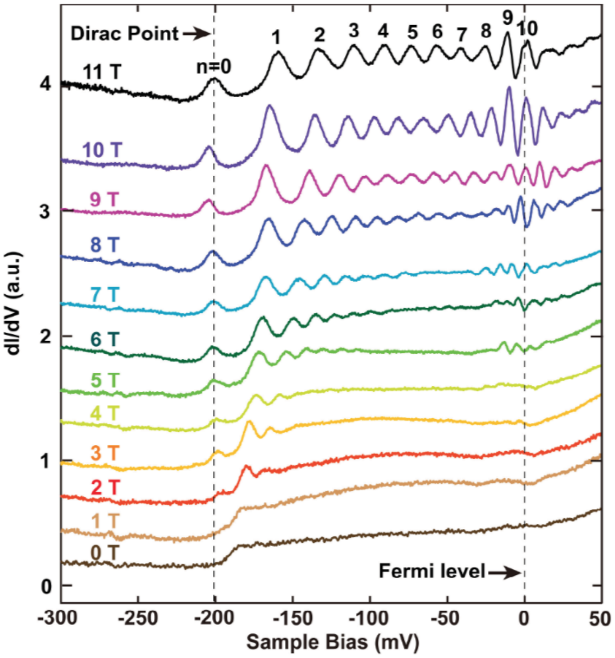

Figure 1.16: Landau levels in the LDOS of Bi_2Se_3. Reprinted from [10] with permission.

Landau levels which are normally suppressed in common materials reappear. Due to the massless property of Dirac electrons, Landau levels in a topological insulator are different from the normal ones. First, the lowest level is always pinned at the Dirac point. Second, the energy of the Landau levels is proportional to $\sqrt{nB}$, where n is the level index and B is the external magnetic field. P. Cheng also verified the 2D nature of these states by depositing silver impurities onto the surface. The observed Landau levels are suppressed when the distance between impurity atoms reaches less than 10 nm, the characteristic magnetic length.

1.4.3 Inelastic Scanning Tunneling Spectroscopy

In addition to an electron tunneling across a barrier without the loss of energy (elastic tunneling), the electron as it tunnels can also excite some mode in the barrier and in the process lose an energy of $\hbar\omega$ (inelastic tunneling). However, if the electron now has an energy corresponding to a filled state, it will not be able to tunnel. Consequently, inelastic tunneling can only occur when the voltage across the barrier is greater than or equal to the excitation energy of the mode, $V \geq \frac{\hbar\omega a}{e}$.

When this condition is met, the inelastic tunneling current adds to the elastic tunneling current. Consequently the conductance, $\frac{dI}{dV}$, will exhibit a step increase as a function of the applied voltage at $V = \frac{\hbar\omega a}{e}$ as shown in Fig. 1.17. The second derivative of the current with respect to the voltage, $\frac{d^2I}{d^2V}$, will exhibit a peak at $V = \frac{\hbar\omega a}{e}$ which is a direct measure of the resonance of the excitation mode. This is the basis of inelastic scanning tunneling spectroscopy (IETS) which has proved capable of measuring the vibrational modes of molecules that are either on the surface of the metals or within the tunneling barrier.

Here, we briefly discuss how a lock-in amplifier (LIA) can be used to extract the conductance and $\frac{d^2I}{d^2V}$. First, one adds a small modulation, $U\cos[\omega t]$, to the voltage applied to the tunnel junction. The resultant tunneling current will be a function of the DC and modulation voltages, $I[V + Ucos[wt]]$. Because U is small, one can expand the current in a Taylor series

$$I[V + Ucos[wt]] = I[V] + \frac{dI}{dV}[V]Ucos[wt] + \frac{1}{2}\frac{d^2I}{dV^2}[V]U^2(cos[wt])^2 \tag{1.29}$$

Noting that $(cos[wt])^2 = \frac{1}{2}(1 + cos[2wt])$ we see that the measured current has a component that oscillates at the second harmonic of the applied modulation.

$$I[V + Ucos[wt]] = (I[V] + \frac{1}{4}\frac{d^2I}{dV^2}[V]U^2) + \frac{dI}{dV}[V]Ucos[wt] + \frac{1}{4}\frac{d^2I}{dV^2}[V]U^2cos[2wt] \tag{1.30}$$

To measure this second derivative term, the LIA outputs the signal intensity at the frequency of 2ω.

$$I_{2\omega} = \frac{2\omega}{\pi}\int_{t=0}^{\pi/\omega} I[V + U\cos[\omega t]]cos[2\omega t]dt \tag{1.31}$$

Substituting $u = Ucos[wt]$, the second harmonic signal becomes

$$I_{2\omega} = \frac{2}{\pi U^2}\int_{-U}^{U} I[V + u]\frac{(2u^2 - U^2)}{\sqrt{U^2 - u^2}}du \tag{1.32}$$

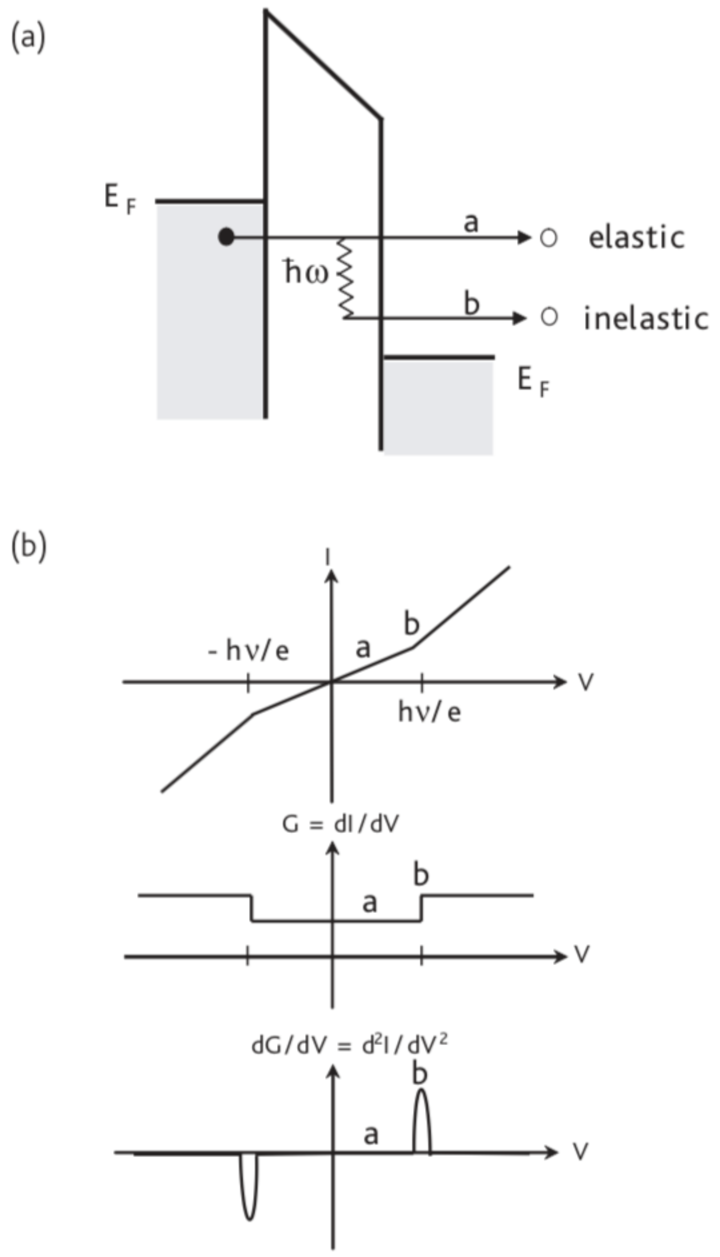

Figure 1.17: Inelastic tunneling process. (a) An illustration of elastic and inelastic tunneling processes. (b) Characteristics of the I, $\frac{dI}{dV}$ and $\frac{d^2I}{dV^2}$ curves as a function of the voltage. Reprinted from [11] with permission.

Integrating by parts twice, we obtain

$$I_{2\omega} = \frac{2}{3\pi U^2} \int_{-U}^{U} \frac{d^2 I[V+u]}{dV^2} (U^2 - u^2)^{\frac{3}{2}} du \tag{1.33}$$

It can be viewed as a convolution between the second order derivative $\frac{d^2I}{dV^2}$ and a function

$$\begin{aligned} \phi(u) &= \frac{2}{3\pi U^2}(U^2 - u^2)^{\frac{3}{2}} \qquad && for|u| < U; \\ \phi(u) &= 0 && for|u| \geq U. \end{aligned} \tag{1.34}$$

Note that a smaller modulation U leads to a smaller broadening. On the other hand, a smaller U also leads to a smaller signal to noise ratio.

In addition to the modulation broadening, there is also a thermal broadening because the second derivative itself is a convolution between the function of $\frac{d^2I}{dV^2}$ at zero temperature and the derivative of Fermi distribution at a finite temperature. The total line width W is given by

$$W^2 = W_I^2 + W_T^2 + W_U^2 \tag{1.35}$$

where W_I is the intrinsic line width of the vibrational mode, W_T is the thermal broadening and W_U is the modulation broadening. From this expression, we see again the importance of carrying out experiments at low temperatures.

1.4.4 Quasiparticle Interference Pattern

By performing a scan while recording the signal of a LIA instead of the voltage on the z piezo, we can construct an image of $\frac{dI}{dV}$ over the surface. In these images, if there are scattering centers of the electrons on the surface, one can observe standing waves with enhanced contrast at some voltages and reduced contrast at others. The Fourier transform of such a $\frac{dI}{dV}$ image is called an quasiparticle interference pattern. Even though people still debate about the principle of these patterns, it is believed to contain information about the scattering vectors of electrons. As shown in Fig. 1.18, T. Zhang et al. [12] obtain this kind of pattern on the surface of Bi_2Te_3 decorated

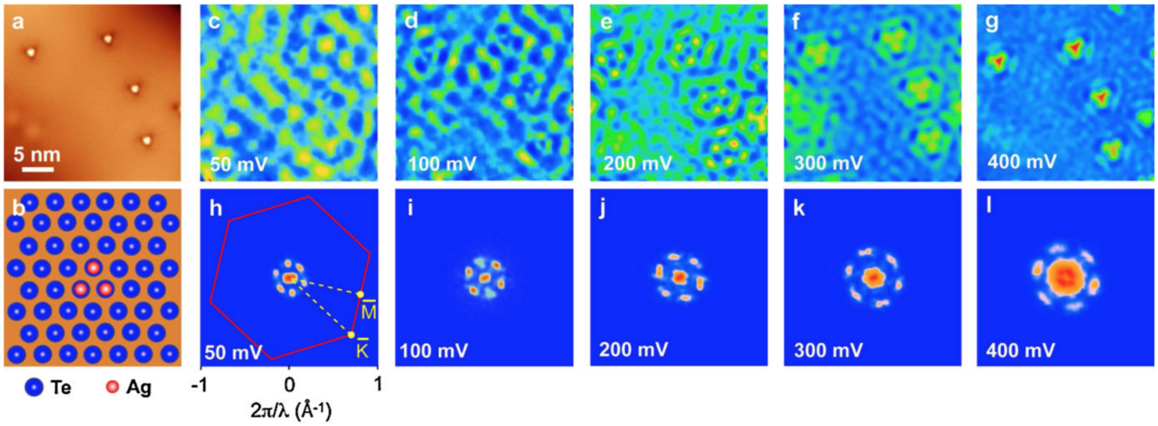

Figure 1.18: Quasiparticle patterns. (a) STM topography of Ag impurities on Bi_2Te_3. (c-g) Standing wave patterns caused by Ag impurities at different bias voltages. (h-l) Fourier transforms of (c-g). Reprinted from [12] with permission.

with dispersed silver atoms on the surface. His results show strong intensities along the $\bar{\Gamma} - \bar{M}$ directions but weak intensities along the $\bar{\Gamma} - \bar{K}$ directions. This observation strongly supports the fact that in a topological insulators, backscattering between $\vec{k}$ and $-\vec{k}$ states are protected because of time reversal symmetry.

1.4.5 Spin-polarized Tunneling

Spin-polarized STM can be realized by coating the tip surface with magnetic materials. Suppose the tip wave functions are given by

$$\Psi_{T\uparrow} = \chi[\mathbf{r}]\begin{pmatrix}1\\0\end{pmatrix}, \qquad \Psi_{T\downarrow} = \chi[\mathbf{r}]\begin{pmatrix}0\\1\end{pmatrix} \tag{1.36}$$

With respect to the tip polarization, the wave functions of the n^{th} atom of the sample can be written as

$$\Psi_{n\uparrow} = \psi_n[\mathbf{r}]\begin{pmatrix}\cos[\theta_n/2]\\ i\sin[\theta_n/2]\end{pmatrix}, \qquad \Psi_{T\downarrow} = \chi[\mathbf{r}]\begin{pmatrix}i\sin[\theta_n/2]\\ \cos[\theta_n/2]\end{pmatrix} \tag{1.37}$$

where θ_n is the angle between the polarization of the tip $\mathbf{e}_T$ and the polarization of the n^{th} atom of the sample $\mathbf{e}_n$, Then the tunneling matrix becomes

$$\hat{M}_n = \begin{pmatrix} M_{n\uparrow\uparrow} & M_{n\uparrow\downarrow} \\ M_{n\downarrow\uparrow} & M_{n\downarrow\downarrow} \end{pmatrix} = M_{n0} \begin{pmatrix} \cos[\theta_n/2] & i\sin[\theta_n/2] \\ i\sin[\theta_n/2] & \cos[\theta_n/2] \end{pmatrix} \tag{1.38}$$

where M_{n0} is the spacial part which does not depend on the spin degree of freedom.

According to the tunneling matrix, the conductance is then

$$G_n = 2\pi^2 G_0(\rho_{T\uparrow}\rho_{n\uparrow}|M_{n\uparrow\uparrow}|^2 + \rho_{T\uparrow}\rho_{n\downarrow}|M_{n\uparrow\downarrow}|^2 + \rho_{T\downarrow}\rho_{n\uparrow}|M_{n\downarrow\uparrow}|^2 + \rho_{T\downarrow}\rho_{n\downarrow}|M_{n\downarrow\downarrow}|^2) \tag{1.39}$$

To see a difference between the normal and the spin-polarized STS, the DOS of opposite polarizations should be different. One can define the spin-averaged DOS, ρ_T and ρ_n, and the spin-polarized DOS, m_T and m_n, as

$$\begin{aligned} \rho_T &= \rho_{T\uparrow} + \rho_{T\downarrow}, \qquad & \rho_n &= \rho_{n\uparrow} + \rho_{n\downarrow} \\ m_T &= \rho_{T\uparrow} - \rho_{T\downarrow}, \qquad & m_n &= \rho_{n\uparrow} - \rho_{n\downarrow} \end{aligned} \tag{1.40}$$

Plugging Eq. 1.40 and Eq. 1.38 into Eq. 1.39, the final tunneling conductance is

$$G_n = \pi^2 G_0|M_{n0}|^2(\rho_T\rho_n + m_T m_n \cos[\theta_n]) \tag{1.41}$$

Clearly, $\rho_T\rho_n$ is the normal tunneling conductance and $m_T m_n \cos[\theta_n]$ depends on the angle between the polarization of the tip and the polarization of atoms on the sample. Therefore, the latter term provides us information about its magnetic properties. Figure 1.19 shows Fe double layer islands on a W substrate. These islands have similar apparent height in a traditional STM image but show clear contrast in a spin-polarized STM image due to their opposite magnetization directions.

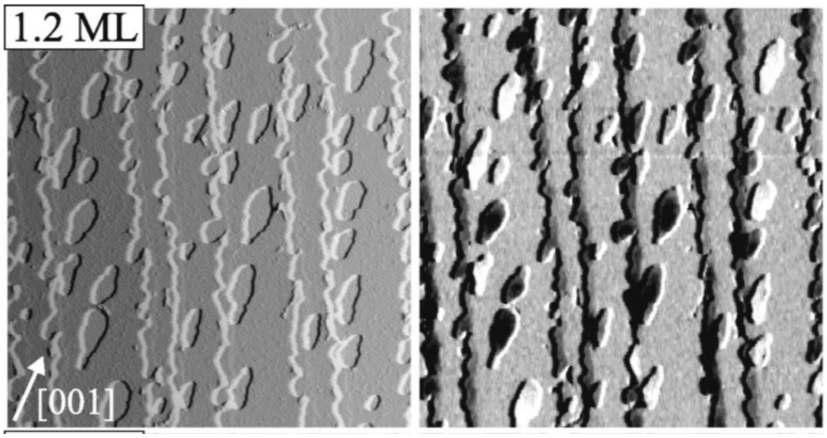

Figure 1.19: Fe double layer islands deposited onto W substrate. Reprinted from [13] with permission.

2. AUXILIARIES FOR THE SCANNING TUNNELING MICROSCOPY

2.1 Pan-Style Coarse Approach

In the introduction section, we introduced four kinds of coarse positioners. Here, we present more details on the Pan-style positioner.

The Pan-style positioner was developed by Dr. S. H. Pan in 1999 [14]. Figure 2.1 illustrates its basic principle. Six piezo feet (only four are shown in the graph) hold the central triangular sapphire prism. In our STM, the feet are made of PZT-8, Model EBL#4 from the EBL Products, Inc. These shear piezo feet are energized one by one while the other five hold the central prism fixed. Then all the feet are relaxed together to move the prism forward. Unlike the Beetle positioner which utilizes inertia to work, this design is very rigid. It is said to be able to move objects as heavy as 1 kilogram up and down in the direction of gravity. Because of its three-fold symmetry, with a proper choice of materials, Pan-style positioner can have very good thermal stability.

The driving voltages of the piezo feet are generated by a BNC-2110 National Instruments multifunctional I/O device. The device is capable of outputting six analog ramp voltages with a peak amplitude of 10 Volts. These small voltages are then amplified by operational amplifiers with a gain of 30. A high voltage power supply provides a voltage of more than 300 volts to the gates of these operational amplifiers. Six outputs from these amplifiers are connected to the positive electrodes of the piezo feet via BNC cables. All six ground electrodes are connected to a single ground of one of the six BNC cables. When the STM is malfunctioning, a good practice is to check the outputs from these amplifiers. Either a problem at the control circuit side or a problem at the cryostat side can distort the outputs. Another important diagnostic test is the capacitances of the piezo feet which can be measured through the BNC cables. Table 2.1 lists the capacitances at room temperature, liquid nitrogen temperature and liquid helium temperature.

Some problems can still develop for the Pan-style coarse positioner at low temperatures. First, at liquid helium temperature, the coefficient of the piezoelectric materials generally has decreased

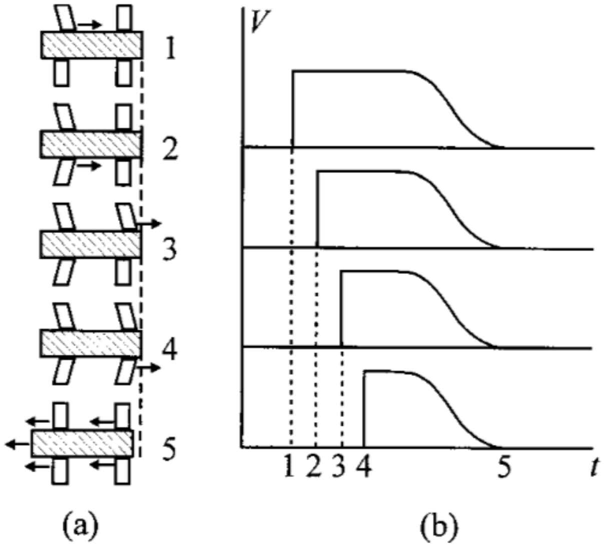

Figure 2.1: Illustration of the principle of a Pan-style coarse positioner. (a) Sequential movements of the piezo feet. (b) The corresponding sequential voltages applied on the piezo feet. Reprinted from [14] with permission.

Temperature	Piezo 1	Piezo 2	Piezo 3	Piezo 4	Piezo 5	Piezo 6
300 K	4158 pF	4263 pF	4214 pF	4022 pF	4235 pF	4236 pF
77 K	2858 pF	2936 pF	2936 pF	2775 pF	2920 pF	2944 pF
4 K	1698 pF	1739 pF	1743 pF	1669 pF	1741 pF	1758 pF

Table 2.1: Capacitances of piezo feet at 300 K, 77 K and 4 K separately.

to one fifth of their value at room temperature. Second, the piezo feet may not be perfectly aligned with the surface of the sapphire prism. Even though well aligned at room temperature, a mismatch of the thermal contraction may still misalign them at low temperature. Third, the titanium body of the STM has a larger thermal contraction than the piezo feet and the sapphire prism. When the temperature decreases, the pressure at the interface between the piezo feet and the prism increases, leading to a larger friction. With too large of an increase of the friction, the coarse approach mechanism may not work in the ideal way described in Fig. 2.1.

At the beginning of this project, the coarse approach mechanism of the STM in our lab failed below 40 K. In order to analyze the problem, a fiber optic interferometer was developed to monitor

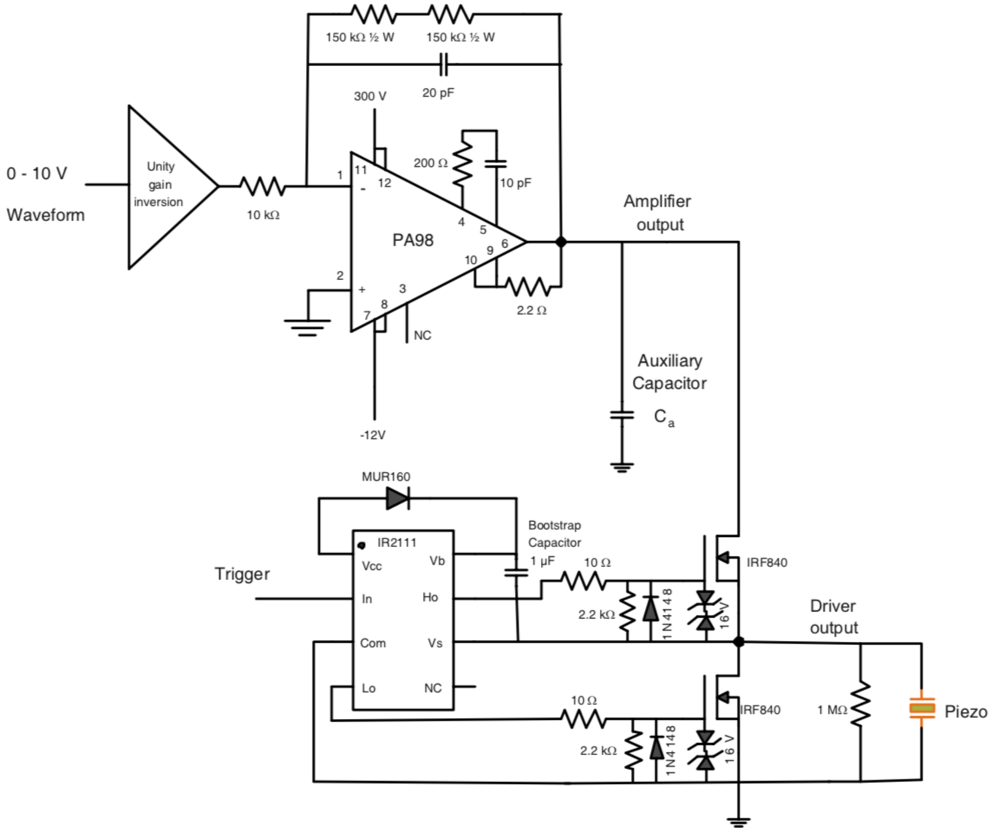

Figure 2.2: The operational amplifier with a bootstrap circuit for controlling the piezo feet. It is safe to cut the two $2.2\,\mathrm{k}\Omega$ resistors at the bottom to have more flexible output waveforms. Reprinted from [15] with permission.

the motion of the coarse positioner.

2.2 Interferometer

Building a LT interferometer presents similar problems as a LT-STM. The sensor arm that bounces a laser beam from the back of the STM is placed in the vacuum can which will be at 4K during experiments. People who have experience in adjusting a light path on an optical stage know the difficulty in obtaining the rigorous requirements on alignment. Therefore, a light path that works at room temperature can easily be distorted as the temperature drops causing the signal to be lost. Another problem is noise. An interferometer can measure displacements on the nanometer scale. As such, it is very sensitive to many forms of noise. The boiling of liquid nitrogen or liquid helium generates mechanical vibrations. Thermal gradients in the optical fiber cause contractions or expansions which change the optical path length. All these potential problems require a careful design and lots of attempts.

Figures 2.3 shows the final design of our working interferometer. The $6419\,\text{Å}$ laser beam is generated by a Melles Griot diode laser. The laser beam is coupled into an optical fiber by a fiber port collimator (Thorlabs, PAF-X-11-633). The beam is then split by a 2×2 single mode fiber coupler (Thorlabs, FC632-50B-APC). A bare fiber (Thorlabs, 630HP-CUSTOM) connects the components outside and inside the cryostat. Both ends of the bare fiber have FC/APC connectors. At some fragile positions, it is covered by some yellow furcation tubing (Thorlabs, FT030-Y). Inside the cryostat, the laser beam is pointed at the STM by an adjustable collimator (Thorlabs, CFC-8X-A). On the STM, a retro-reflector reflects the laser back (Thorlabs, PS974-A). A photon detector measures the interference signal (Thorlabs, PDA55).

Some details are worth mention. In order to reduce the noise in the reference arm, the optical honeycombed breadboard is placed on one arm of the upper support platform of the cryostat. In turn, this platform is isolated from ground vibrations by 3 TMC air vibration isolators that sit on the support tripod. Figure 2.4 is a sketch of the components on the optical breadboard. All optical components are directly fixed to the breadboard without using posts so that they are more rigid. Any extra length of the fibers are coiled to be compact and are covered by teflon tapes to reduce

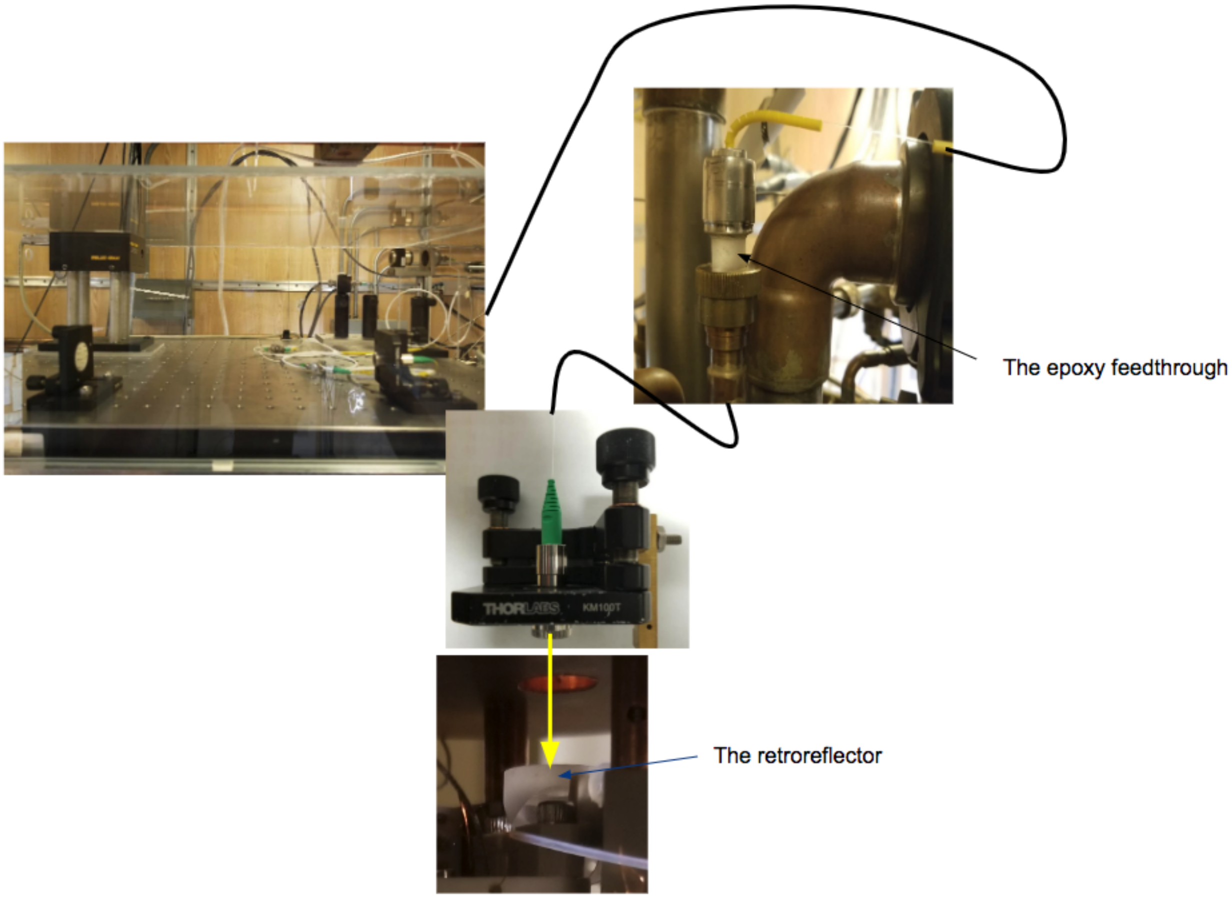

Figure 2.3: The interferometer. The black lines stand for optical fibers. The yellow arrow is a laser beam coming out of the lens.

the influence of temperature. A large, clear plexiglass box surrounds the entire breadboard and the only opening is for the outgoing fibers in order to isolate the system from the external environment.

A vacuum feedthrough for the fiber was made of epoxy Stycast 1266. First, the mixed epoxy is poured into a cylinder container. After it has hardened, it was machined to a diameter corresponding to the o-ring of the Cajoun connector at the top of the cryostat. A through hole was drilled that allows the head of the fiber connector to pass. In order to make a good vacuum seal, a bare fiber without a jacket was used. Because the bare fiber is easy to break, extra care must be taken during the whole assembly process. Once the fiber goes through the hole, mixed epoxy is poured back into the hole to seal it. In order to keep the epoxy from dripping out, two semicircle teflon plugs

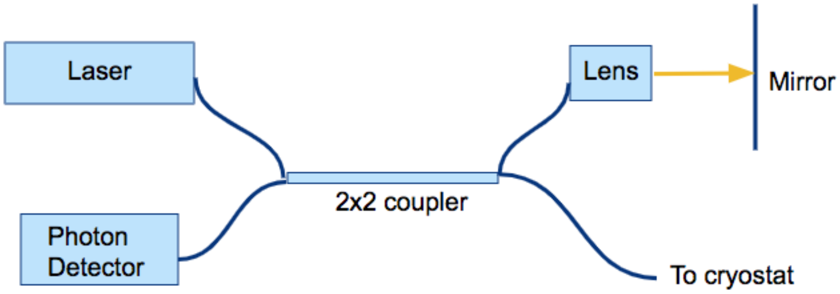

Figure 2.4: Components of the interferometer on the optical stage at the top of the cryostat.

are machined into the right shape to block the bottom of the hole. Before the epoxy is hardened, some plastic jackets are twisted around the fiber at the two ends for strain relief.

The head of the sensor arm is the most critical part of the interferometer. We tried a number of different ideas to reflect the laser beam from the STM including coating the end of an optical fiber with silver to create a semi-transparent mirror. The final design contains an adjustable lens to collimate the outgoing laser beam and a retro-reflector fixed on the STM to reflect the beam back. To get the maximum available signal, one has to make sure that the lens outputs a parallel beam. In other words, the core of the fiber should be at the focal point of the lens. To ensure this requirement is satisfied, the lens should be adjusted so that the diameter of the outgoing beam is a constant at different distances from the lens. The use of the retroreflector instead of simple mirror allows a larger tolerance on the precision of the alignment of all the components. In particular, this solves the problem of distortion caused by thermal contraction.

Figure 2.5 shows the signal during one coarse approach step measured by the interferometer. The blue curve is the ramp voltage applied on one of the six piezo feet. The orange curve is the signal measured by the photon detector. As mentioned previously, during the high plateau of the ramp voltage, the six feet shear one by one while the other five hold the sapphire prism fixed. Clearly, the true situation is different from the ideal expectation. Even moving only a single foot can also move the prism. During the decreasing ramp of the voltage, the six piezo feet are relaxed

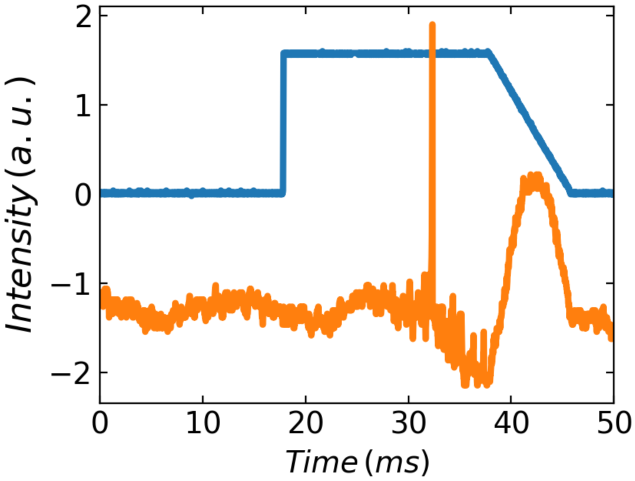

Figure 2.5: Interferometer signal during a single coarse approach step. The orange curve is the signal and the blue curve is the ramp voltage applied to one of the piezo feet.

together and the prism is moved forward. This corresponds to the smooth sine section of the signal.

The signal from the interferometer should be a sine function if the prism constantly moves in one direction. Therefore to make the signal quantitatively analyzable, we must know both the maximum and the minimum intensity. Because a single step is not usually far enough for the signal to reach both the maximum and the minimum, one must perform several successive steps in order to extract these parameters. Taking the signal in Fig. 2.5 as an example, the analysis is a follows.

Figure 2.6 shows a signal of ten successive steps repeating the single step in Fig. 2.5. From it, we know the maximum intensity is 0.23 a.u. and the minimum is -2.89 a.u.. Then the average DC signal is -1.33 a.u. and the amplitude is 1.56 a.u.. When all the piezo feet are relaxed together, the signal increases from -2.07 a.u. to the maximum of 0.23 a.u. and then drops to -1.39 a.u.. Because both the starting and the ending intensity is below the average, the total change of the optical path is half of the wavelength plus two additional segments which can be calculated using the inverse trigonometric function.

$$L = \frac{\lambda}{2} + \frac{\lambda}{2\pi}(arcsin[\frac{|Starting - Average|}{Amplitude}] + arcsin[\frac{|Ending - Average|}{Amplitude}]) \tag{2.1}$$

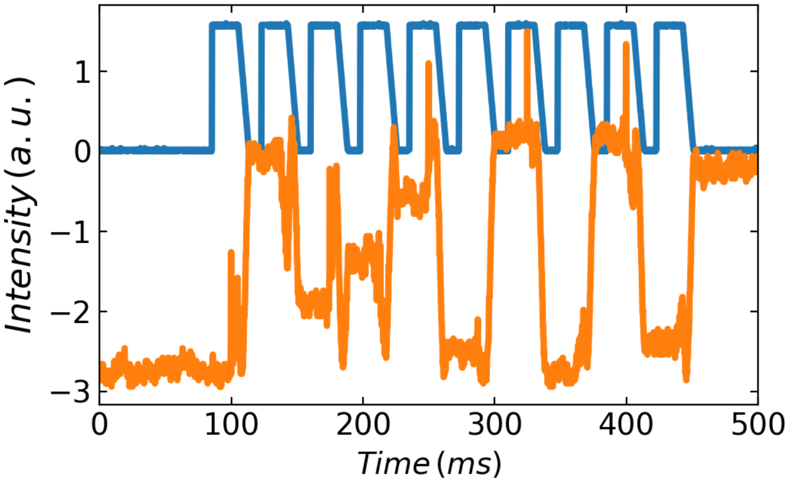

Figure 2.6: Interferometer signal for ten continuous coarse approach steps. The orange and the blue curves are again the signal and the ramp voltage.

where "$Starting$" and "$Ending$" stands for the starting and ending values of the signal. "$Average$" and "$Amplitude$" are as mentioned above. λ is the wavelength of the laser beam (649.1 nm). Plugging in values, we obtain $L = 375.4nm$. Because the laser beam travels back and forth, the displacement of the prism is half of the change of the optical path, 187.7 nm. Dividing by the voltage of 150 V, the coefficient of these piezo feet is therefore 1.25 nm/V.

Then we examine the unexpected reverse motion when each piezo foot is stimulated individually. This corresponds to the plateau of the ramp voltage and the noisy section of the interferometer signal. We can see that the original value of the interferometer signal is at -1.24 a.u. which drops to -2.05 a.u. after all the six feet are sheared sequentially. Because the signal passes the average, the change of the optical path can be calculated by adding two sections which are both shorter than a quarter of the wavelength.

$$L = \frac{\lambda}{2\pi}(arcsin[\frac{|Starting - Average|}{Amplitude}] + arcsin[\frac{|Ending - Average|}{Amplitude}]) \tag{2.2}$$

where "$Starting$" and "$Ending$" are the starting and ending values of the current section. Plugging in values, we get $L = 54.9nm$. Therefore, the displacement is 27.5 nm. This represents a 15%

backslide of the 187.7 nm. The net displacement of the prism becomes $187.7 - 27.5 = 160.2nm$. To reduce the variance for the net step size estimation, sequential steps can be taken. Then the net step size is the total distance divided by the number of steps.

By carefully analyzing the processes depicted in Fig. 2.1, the reverse motion caused by an individual foot can be understood. After the first foot shears, the prism is balanced by the friction of this first foot against the total friction of all the others. In order to provide this friction, the first foot will not reach its unconstrained shear angle and the other five feet will also shear a little. Because there should be no relative motion between the prism and the five static feet, the prism also moves. After the second foot shears, the prism is balanced by the friction of the two already triggered feet and the total friction of the other four. Therefore, the burden on the first foot reduces. It will shear more, dragging the prism. In other words, the real situation is a much more complex than the ideal one. The smaller the friction is, the closer it is to the ideal case. However the friction should be at least large enough to hold the prism against gravity.

The displacement per volt parameter during the decreasing ramp of the voltage should be an intrinsic parameter of the positioner. It only depends on the temperature and not on the vagaries of the static and sliding frictions of the feet. But the reverse backsliding motion depends on a number of factors like the temperature, the pressure applied to the piezo feet and even the precision of the machined components. These two components of a single step can be measured at different temperatures for both upward and downward motions. Figure 2.7a and 2.7b plot these components as a function of the temperature. Figure 2.7c shows the net step size versus temperature. Applying only a voltage of 150 V, the reverse backsliding motion does indeed cancel the forward motion. This may be the reason for the previous failure of the positioner. However, by applying a voltage of 230 V, the positioner works well from room temperature down to $1.6\,\mathrm{K}$.

From these graphs, one can make several conclusions. The displacement per volt measured from upward and downward steps are very similar as expected becaue it should be an intrinsic parameter of the positioner. Our measurements for the displacement per volt as a function of temperature also agrees reasonably well with the piezoelectric constant of the PZT-8 provided by

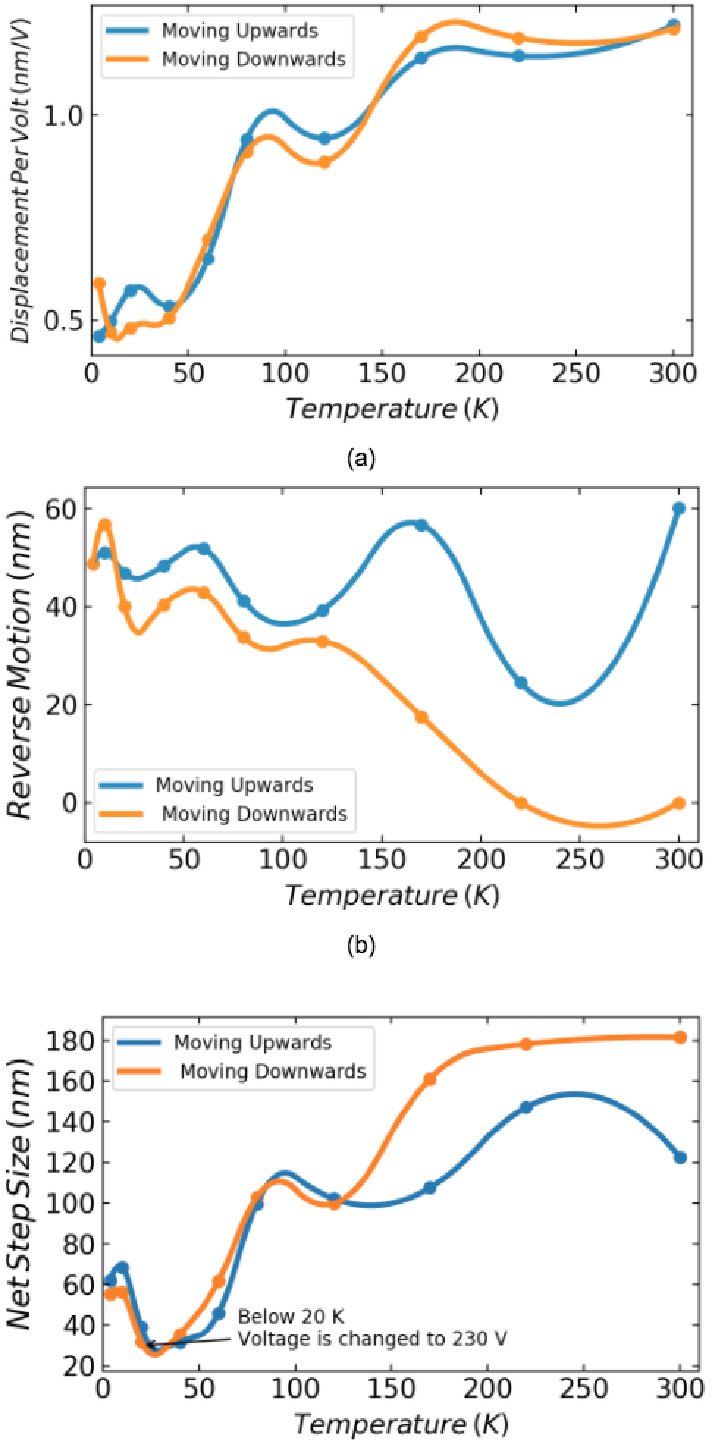

(a)

(b)

(c)

Figure 2.7: Parameters of the piezo feet calculated from the data of the interferometer at different temperatures. (a) Displacement per volt. (b) Reverse motion due to imperfections. (c) Net step size.

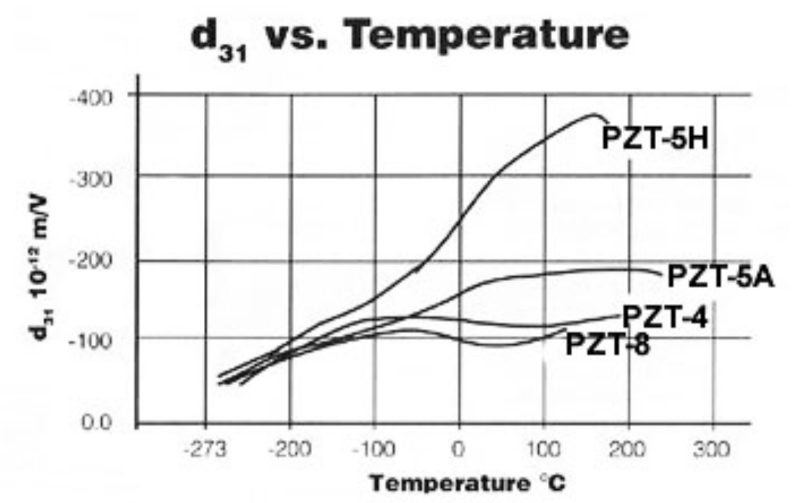

Figure 2.8: Temperature dependence of the piezo coefficients of four common commercial piezoelectric materials. Adapted from the website of the Boston Piezo Optics Inc..

the EBL Products, Inc. (see Fig. 2.8). Specifically, the coefficients both have a maximum at around 190 K.

Note that the reverse backsliding motions are different for upward and downward steps. At high temperatures, the upward step has a very large reverse backsliding motion whereas the downward step has a small one. This is due to gravity. At low temperatures, when friction is much larger than gravity, the reverse backsliding motion of upward and downward steps are approximately the same.

The z extension per volt for the tube scanner of our STM was also measured as a function of the temperature. After a tunneling current is detected, one can move the sapphire prism for a single step up or down. The feedback system will then adjust the z voltage on the tube scanner to stabilize the current. Dividing the measured step size by the change of z voltage gives the extension per volt of the tube scanner. As can be seen from Fig. 2.9, the extension per volt for the tube scanner has a similar temperature dependence as the PZT-8 used to make the piezo feet.

2.3 Eddy Current Damper

Eliminating mechanical vibration is critical for an STM. The shielding room in our lab sits on a 6 inch thick slab of concrete that is isolated from the floor by springs. The frame on which the

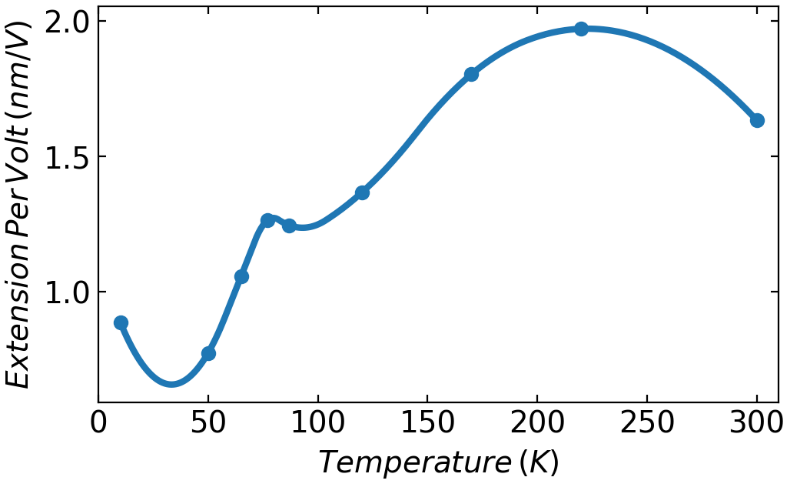

Figure 2.9: Temperature dependence of the extension per volt of the tube scanner.

cryostat sits is further isolated from the floor of the shielded room by three TMC high pressure gas vibration isolators. The mechanical pumps are placed in a another room that is separated by two walls. The pumping lines have flexible sections to avoid propagating vibrations. Unfortunately, the STM is mounted at the bottom of a long, free hanging cryostat. To further reduce vibration, an eddy current damper was built.

Figure 2.10 is a picture of the eddy current damper. The STM is supported by three Inconel springs below the ^{3}He stage. The STM spring system behaves both as a spring system and a pendulum whose resonant frequencies are given by $\omega = \sqrt{\frac{k}{m}}$ and $\omega = \sqrt{\frac{g}{l}}$ respectively. For springs made from the same material with the same diameter, a longer length leads to a smaller spring constant k. Therefore, in order to achieve lower resonance frequencies longer springs are always preferred as long as they fit within the limited space inside the vacuum can.

When the STM stage vibrates relative to the oxygen-free high conductivity copper (OFHC) plate (located above the STM stage), the magnets on the STM stage will generate an eddy current in the plate. This current will be transformed to heat by the resistance and the motion of the plate is dissipated. Effectively, the spring system works as a low pass filter and the eddy current damps the relative motion between the STM stage and the plate. Notice that there are three pairs of magnet.

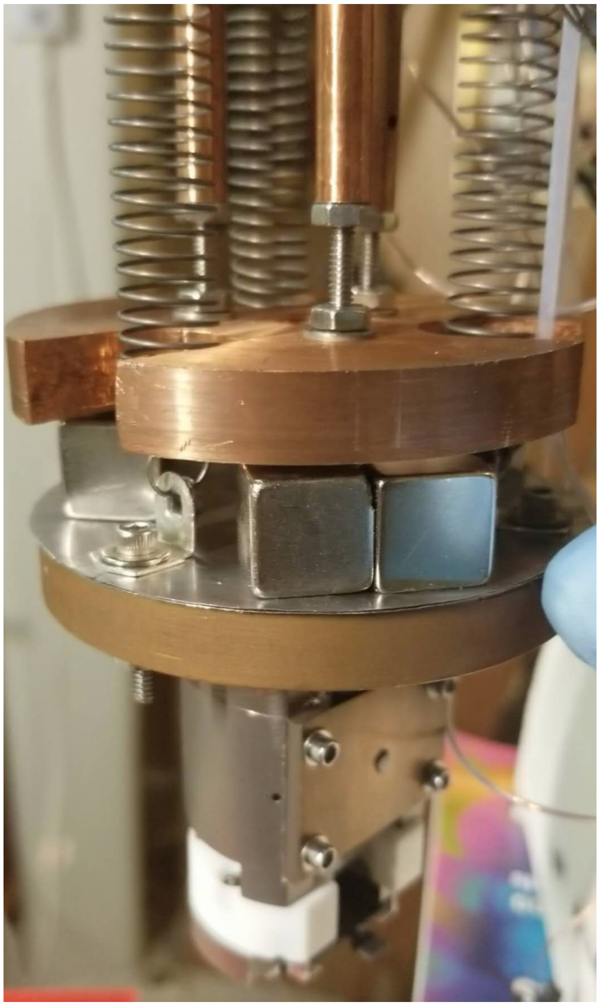

Figure 2.10: Picture of the eddy current damper.

To achieve the best damping effect in both horizontal and vertical directions, the two magnets in a pair have opposite magnetic fields.

To understand how this system acts as a low pass filter, one can model the whole system as a 1D mass-spring system with a damping force as shown in Fig. 2.11. Suppose the mass is a distance S from the balance point of the spring. The elastic force exerted by the spring is $-kS$ and the damping force is $-\mu(\frac{dS}{dt} - \frac{dM}{dt})$, where $\frac{dM}{dt}$ is the speed of the magnet. Generally, the magnetic field of a magnet is very nonuniform. Therefore for large vibrations, μ is not a constant. However for our system, the vibrations are usually microscopic and invisible to the eye. For this reason, μ can be treated as a constant. In practice, to enhance the effect of the damper, the magnets should

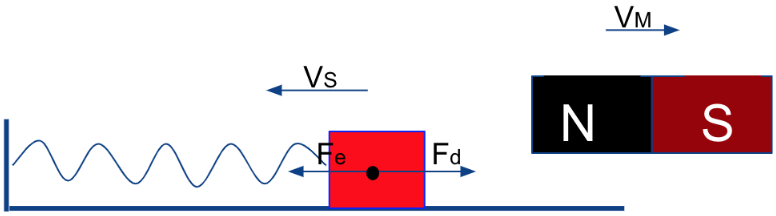

Figure 2.11: A simple sketch of the eddy current damper in 1D.

be placed as close as possible to the OFHC plate. To simplify the derivation, we take $m = 1$. Then Newton's second law for the system is

$$\frac{d^2S}{dt^2} = -kS - \mu\left(\frac{dS}{dt} - \frac{dM}{dt}\right) \tag{2.3}$$

For a given frequency ω

$$\begin{aligned} S &= B_1 \sin[\omega t] + B_2 \cos[\omega t] \\ M &= A_1 \sin[\omega t] + B_2 \cos[\omega t] \end{aligned} \tag{2.4}$$

Then the corresponding velocities and accelerations are

$$\begin{aligned} \frac{dS}{dt} &= B_1\omega \cos[\omega t] - B_2\omega \sin[\omega t] \\ \frac{dM}{dt} &= A_1\omega \cos[\omega t] - B_2\omega \sin[\omega t] \\ \frac{d^2S}{dt^2} &= -B_1\omega^2 \sin[\omega t] - B_2\omega^2 \cos[\omega t] \end{aligned} \tag{2.5}$$

Plugging Eq. 2.5 into Eq. 2.3, we obtain

$$((k-\omega^2)B_1 - \mu\omega B_2 + \mu\omega A_2)\sin[\omega t] + ((k-\omega^2)B_2 + \mu\omega B_1 - \mu\omega A_1)\cos[\omega t] = 0 \tag{2.6}$$

Because the equation should be satisfied for all t, the coefficients before the $\sin$ and $\cos$ functions should be zero, leading to

$$\begin{aligned}(k-\omega^2)B_1-\mu\omega B_2+\mu\omega A_2&=0\\(k-\omega^2)B_2+\mu\omega B_1-\mu\omega A_1&=0\end{aligned}\tag{2.7}$$

Solving this set of equations we obtain

$$\begin{aligned}B_1&=\frac{\mu^2\omega^2A_1-\mu\omega(k-\omega^2)A_2}{(k^2-\omega^2)^2+\mu^2\omega^2}\\B_2&=\frac{\mu\omega(k-\omega^2)A_1+\mu^2\omega^2A_2}{(k^2-\omega^2)^2+\mu^2\omega^2}\end{aligned}\tag{2.8}$$

and the squared amplitudes of the vibrations are

$$\begin{aligned}B_1^2+B_2^2&=\frac{(k-\omega^2)^2\mu^2\omega^2+\mu^4\omega^4}{[(k-\omega^2)^2+\mu^2\omega^2]^2}(A_1^2+A_2^2)\\&=\frac{\mu^2\omega^2}{(k-\omega^2)^2+\mu^2\omega^2}(A_1^2+A_2^2)\end{aligned}\tag{2.9}$$

Therefore, the coupling efficiency between the STM stage and the plate becomes

$$\frac{\sqrt{B_1^2+B_2^2}}{\sqrt{A_1^2+A_2^2}}=\frac{\mu\omega}{\sqrt{(k-\omega^2)^2+\mu^2\omega^2}}\tag{2.10}$$

Figure 2.12 illustrates the coupling efficiency as a function of the frequency for $k=\mu=1$. It is clear that the whole system is a low pass filter. As a reference, three Inconel springs of $1\,\mathrm{cm}$ diameter, $3.5\,\mathrm{cm}$ natural length, and $30\,\mathrm{N/m}$ spring constant are used in the system. Because the STM body itself is made from very stiff materials like titanium, sapphire, stainless steel and PZT, that are ridgidly connected, the STM body acts as a high pass filter. Together with the eddy current damper, external vibrations can be effectively suppressed. Figure 2.13 shows the spectra of the tunneling current measured on an atomically flat gold surface before and after the eddy current damper was implemented. A clear drop in the amplitude of the vibrations is shown. The orange curve which shows the spectrum at low temperature without the eddy current damper, is actually better than the spectrum at room temperature. This can be understood as a result of materials

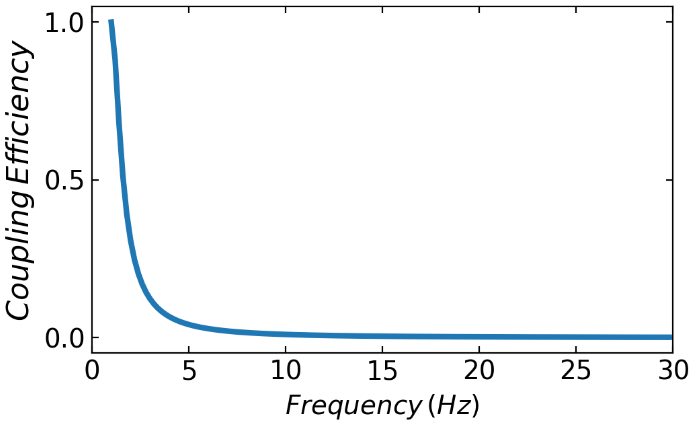

Figure 2.12: The coupling efficiency of the eddy current damper system versus the vibration frequency.

getting stiffer at low temperature. In addition, the dewar adds mass to the cryostat, reducing the resonant frequency of the air isolator system and the dewar shields the cryostat from external acoustic noise. This is encouraging because we may not be able to use the eddy current damper in some cases such as for experiments requiring magnetic fields.

2.4 Moving Sample Stage

During an experiment, the ability to move the sample is often necessary. If an atomic resolution image is desired for non-layered materials, even after an in-situ cutting, a flat enough area is unlikely to appear within the micrometer scale window directly reachable by the scanner. A concentric tube scanner can expand the covered window, but in order to obtain the capability of scanning within a millimeter area, a flexible sample stage is needed. Although a piezo-based stage is more reliable and accurate, a mechanical stage is easier to design and construct.

Figure 2.14 is a picture of the mechanical sample stage in our lab which unfortunately only allows 1D movement. At the top of the cryostat, a stainless steel wire can be rolled up by a spindle. The spindle can be rotated from the outside of the vacuum space. Two o-rings in series provide the vacuum seal. The two meters long wire transmits the motion to a brass disk in front of the STM. A #2-56 screw rotates together with the disk. The head of the screw then pulls or pushes

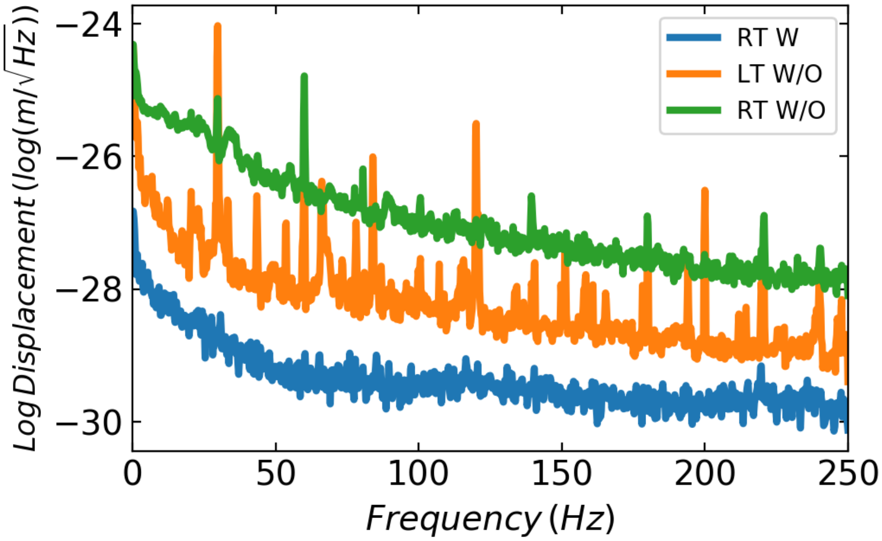

Figure 2.13: Spectra of the tunneling current in different situations. The meanings of the legends are: RT W: Room temperature with the eddy current damper; LT W/O: Low temperature without the eddy current damper; RT W/O: Room temperature without the eddy current damper.

the sample stage. A loaded spring attached to the other end of the wire makes reverse motion possible. When the wire is released by the spindle, the spring will pull the wire causing the disk to rotate in the opposite direction.

Two parameters control the transformation of the large rotational motion of the spindle to a small linear motion of the sample stage. First, the spindle has a diameter of 0.35 inch while the brass disk is 0.5 inch. This is a ratio of 0.7. Second, because a #2-56 screw is used, one revolution of the disk results in a 0.45 mm linear displacement. In total, if the spindle is rotated by $10°$, the sample will be moved by

$$d = \frac{10}{360} \times 0.7 \times 0.45 = 8.75 \times 10^{-3} mm = 8.75 \mu m \tag{2.11}$$

One could decrease the motion per revolution by increasing the threads per inch and by changing the ratio of the diameters of the spindle and the brass disk. Commonly used screws can reach up to 160 threads per inch. If we can decrease the diameter of the spindle to 0.2 inch and increase the diameter of the brass disk to 0.7 inch then rotating the spindle by $10°$ will move the sample by

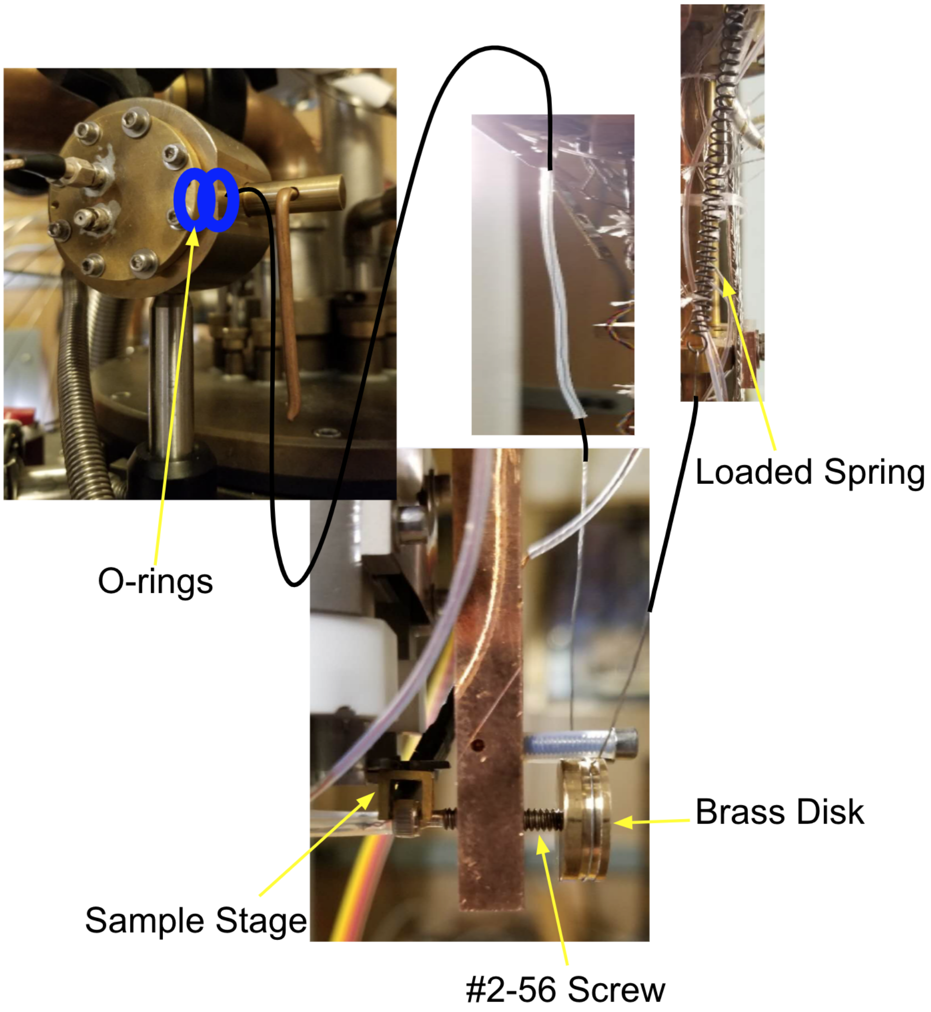

Figure 2.14: The moving sample stage. The black lines stand for the stainless steel wire.

$1.2\mu m$. Because the scan window of the STM is a $2.3\mu m$ square, a step size of $1.2\mu m$ would be a fine enough.

The total travel range of the sample stage is limited by how long the spring can be stretched. The spring was carefully chosen so that it can provide a large enough force to pull back the wire but not so strong that it cannot be stretched. Stretching the current spring by 3 inches, one can achieve a 0.86 mm travel range.

There are some details of the mechanical sample stage worth mentioning. The stainless steel wire is encased in a Teflon tube when it goes through the pumping line. This is firstly to reduce

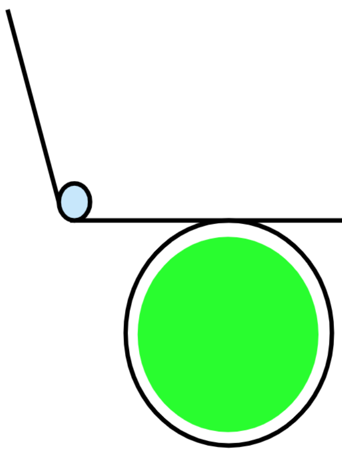

Figure 2.15: Two posts right above the copper disk keep the stainless steel string horizontal.

unnecessary friction and secondly to avoid unexpected damage due to the sharpness of the wire. Figure 2.15 shows the brass disk. Note that there are two posts guiding the wire so that they touch the plate horizontally. This ensures that no net force is exerted by the wire to the disk but only a torque. Otherwise, the screw could get stuck and would be unable to rotate. The head of the screw loosely fits in a groove which is glued onto the sample stage. This allows the screw to be decoupled from the sample stage after finishing its task, avoiding propagating vibration. The groove is glued to the sample plate by a nonconductive epoxy H74F, so that the sample plate is kept electronically isolated.

2.5 Electronic Noise

Electronic noise is harder to eliminate than mechanical noise because it is everywhere. External signals can couple into the measurement system in three ways i.e. capacitive coupling, inductive coupling and ground loops.

2.5.1 Capacitive Coupling

Any ambient electric field can induce a voltage in the electronic circuit. This is one of the reasons why the metal shells of electronic products are grounded. In a similar way, coaxial cables can be used to reduce this kind of noise. Figure 2.16a shows a circuit with bare cables. The

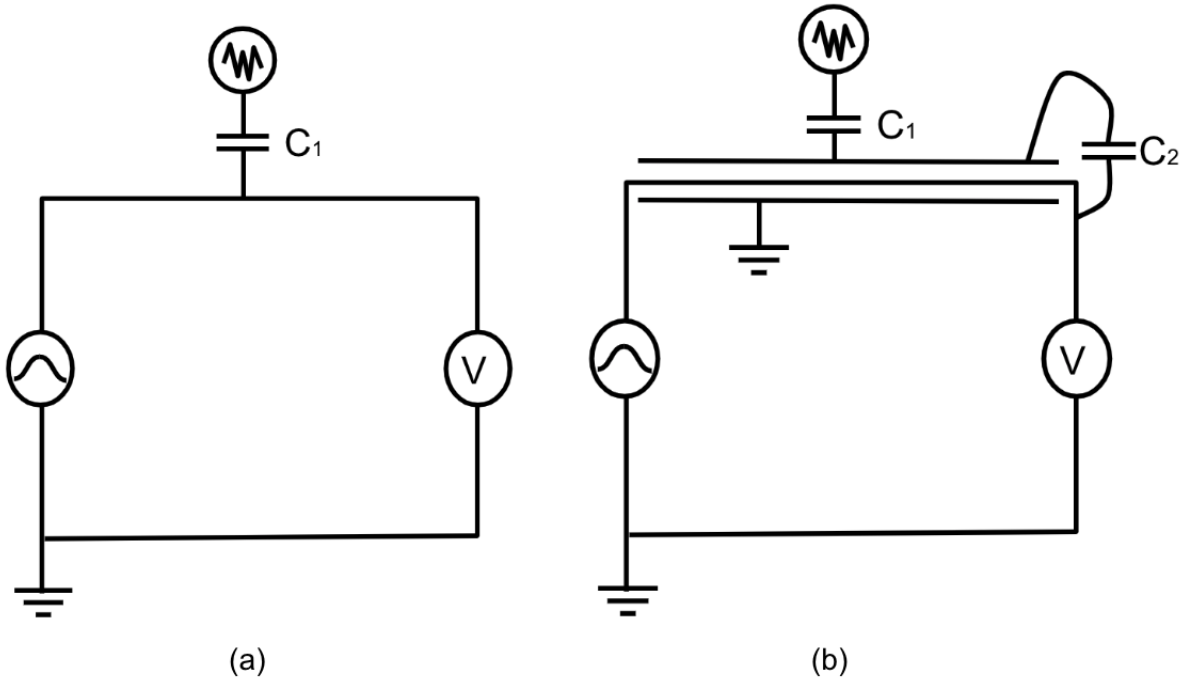

Figure 2.16: Illustration of capacitively coupled electronic noise. (a) The circuit is comprised of bare cables. (b) The circuit is comprised of coaxial cables.

AC noise V is directly coupled into the circuit through a capacitance C_1 and ideally the voltage measured by the voltmeter should be V. Figure 2.16b shows a circuit comprised of coaxial cables. Here the noise V is coupled into the shielding first through the capacitance C_1. Although the noise signal is still coupled to the inner conductor of the coax through C_2, it is easier for the current to flow directly to the ground. Therefore, the coaxial cable can greatly reduce the capacitive noise. However, the capacitance can still introduce thermal noise as will be described in Section 2.5.4.

Another way to eliminate capacitively coupled noise is to shut down the source. In the environment of a laboratory, the major source of spacial electric fields is the fluorescent lights and their power supplies and therefore it is often necessary to shut them down during experiments.

2.5.2 Inductive Coupling

As illustrated in Fig. 2.17, the ambient changing magnetic fields can also cause a voltage drop in the circuit due to the Faraday effect. An effective way to reduce inductively coupled

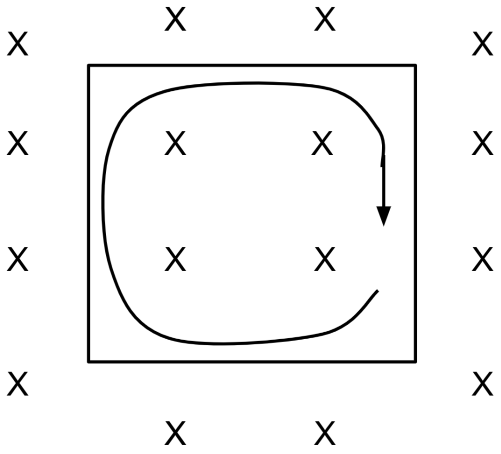

Figure 2.17: Changing magnetic field generates current in a closed loop. Crosses are magnetic fields going into the plane. Supposing a decreasing field, the arrow shows the direction of the current.

noise is to use twisted pairs of wires. This is especially important for wires used to measure the resistances of thermometers. These thermometers are usually several ohms at room temperature and are connected to a resistance bridge or a temperature monitor via wires of hundreds of ohms in order to reduce the amount of heat conducted down the cryostat from room temperature. To measure the resistance of the thermometers in the presence of the resistances of the connecting wires, a four wire configuration is used. In order to prevent the self-heating of the thermometers, a very small current usually less than $1mA$ is applied. The usage of twisted pairs helps to reduce the noise that could overwhelm the input amplifiers of the resistance bridges.

2.5.3 Ground loop

As illustrated in Fig. 2.18, if the signal source and the signal reading device are plugged into separate power outlets, a large current generated by some nearby device like a motor or a heater can flow through the wire between them. This current produces a voltage drop IR between the grounds of the two devices.

Suppose the signal generated by the source is V_S and the voltage on the ground line is V_S^+. Then the voltage on the central conductor at the source side is

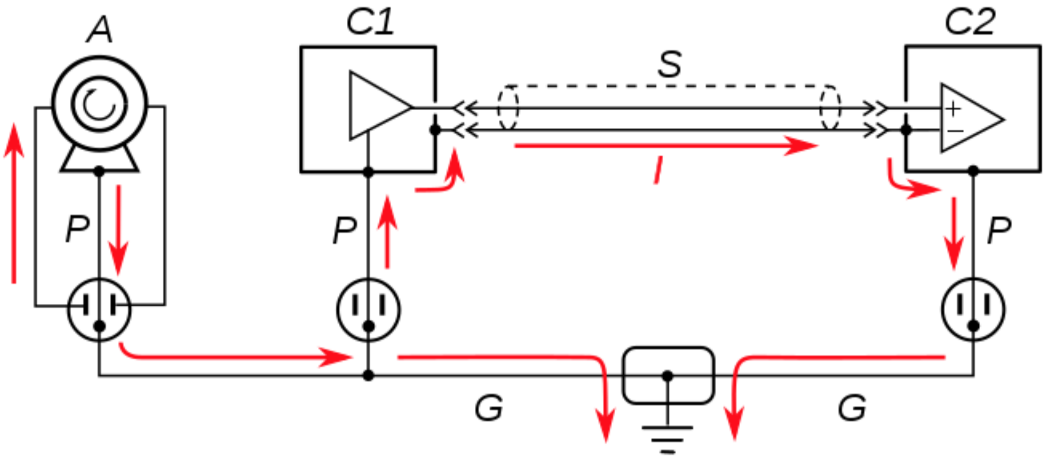

Figure 2.18: Illustration of a ground loop. Reprinted from [16]. Permission is not required for reprint.

$$V_S^+ = V_S^- + V_S \tag{2.12}$$

and the voltage drop on the ground line is

$$V_O^- = V_S^- - IR \tag{2.13}$$

If there is no current flowing through the central conductor, we have

$$V_O^+ = V_S^+ \tag{2.14}$$

The actual signal measured will be

$$V_O = V_O^+ - V_O^- = V_S^+ - V_S^- + IR = V_S + IR \tag{2.15}$$

which is different from the signal by a value of IR.

Ground loop usually appears as a 60 Hz noise on the tunneling current. To get rid of it, one needs to plug all devices into the same power strip or in the case that one power strip is not enough, all devices should be plugged into close power strips. Another helpful method is to gap

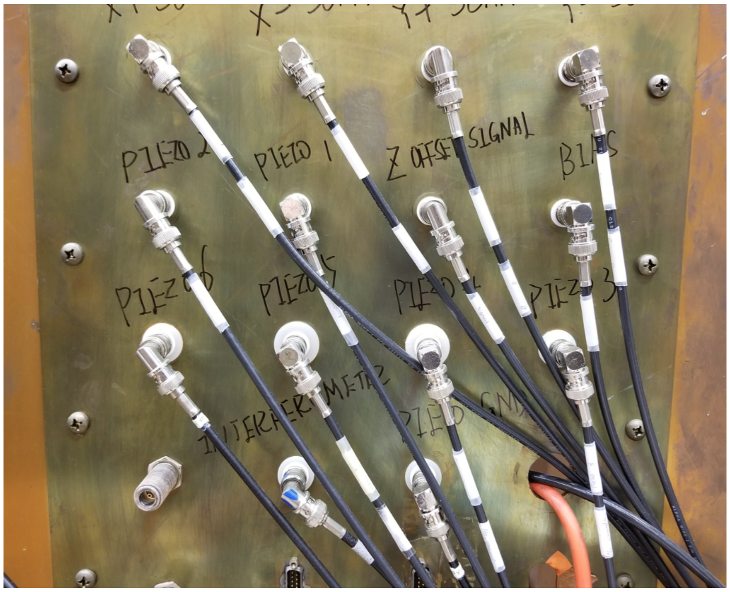

Figure 2.19: BNC cables carrying STM control voltages.

the shielding of the coaxial cables to prevent current from flowing through them as long as one makes sure that the two separate sections of the shielding are still grounded. Figure 2.19 shows all the BNC cables that carry voltages to control the piezoelectric components of the STM. Their shielding is all gapped.

2.5.4 Thermal Noise

Thermal fluctuations can generate noise on a capacitor. Therefore, the capacitance of the coaxial cable connecting the STM tip to the current preamplifier causes problem. One solution is to have a current amplifier that is able to work at liquid helium temperature. In this way, it can be placed very close to the STM. An alternative solution is to have a cable of a larger diameter and thus a smaller capacitance. Third, because this kind of noise is at a higher frequency than the signal, it can be removed by a low pass filter.

Thermal fluctuation induced capacitive noise can be found on all coaxial cables. The noise on the cable for the bias voltage is harmless because the noise is only millivolts. However it may cause problems for the cables that carry the scanning voltages of the tube scanner. The displacement per volt of the tube scanner in the x and y directions are approximately $10\,\mathrm{nm/V}$. A $10\,\mathrm{mV}$

noise can therefore cause a vibration of $1\,\text{Å}$ which can be an issue in achieving atomic resolution. Fortunately, in our system, we have obtained atomic resolution images for several different samples without considering this problem. The tunneling current does have high frequency noise, which can be partly caused by this vibration. Perhaps the low pass filter of the current amplifier automatically solves the problem.

2.5.5 Stray Field of Piezo-driving Voltages

When the tip is being scanned, four high volage sine waves are applied on the x and y electrodes of the tube scanner. These signals can be picked up by the tip adding noise to the tunneling current. In order to alleviate this problem, we enclose all the copper wires of the STM in copper nickel tubes. This includes the five wires for the tube scanner and the nine for the piezo feet. These tubes are all grounded to the titanium body of the STM to provide shielding.

After all the efforts mentioned above, the electronic noise was greatly reduced. Figure 2.20a compares the current noise in the time domain and Fig 2.20b compares the noise current in the frequency domain.

After all the improvements, the STM is able to produce high quality atomic resolution images. The image of graphite is shown in Fig. 1.11. Figure 2.21 shows the image of self assembled dodecanethiol monolayer on gold.

2.6 Operation of the ^{3}He Cryostat

2.6.1 Preparation

1. The resistances of all the thermometers, heaters and samples should be checked before closing the vacuum can. Similarly, the resistances of the helium level detector and the bath resistor should be checked before raising the bath. The relative positions between the level detector, 1K pot inlet valves, magnet and 4K flange should also be recorded before raising the bath. Table 2.2 lists the resistances for some of the thermometers, heaters and level detectors at room temperature for reference.

   Thermometers starting with the letter C are carbon glass thermometers. Ge22726 is a ger-

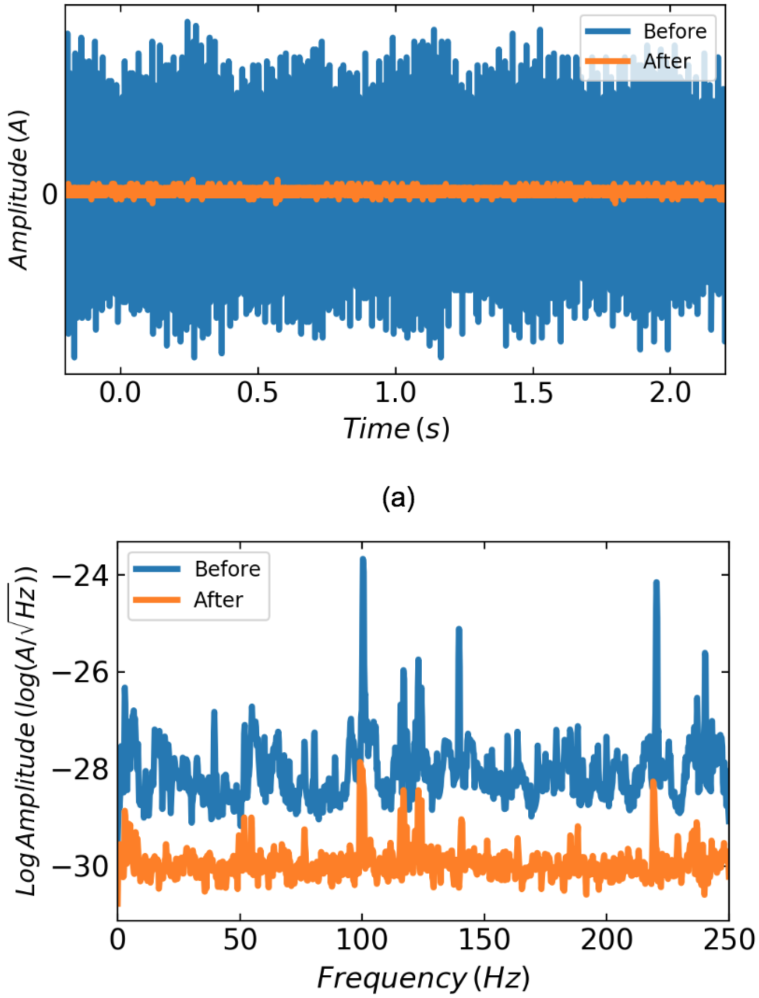

(a)

(b)

Figure 2.20: Comparison of the noise levels before and after all the improvement mentioned above. (a) The current signals. (b) The spectra of the current.

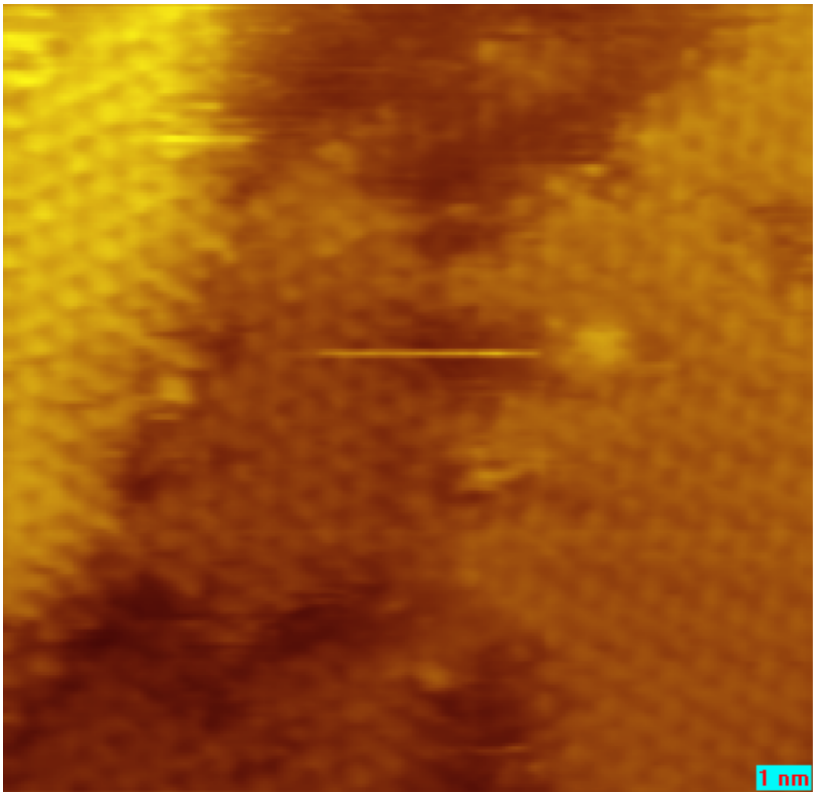

Figure 2.21: Atomic resolution image of self assembled dodecanethiol monolayer on a gold surface.

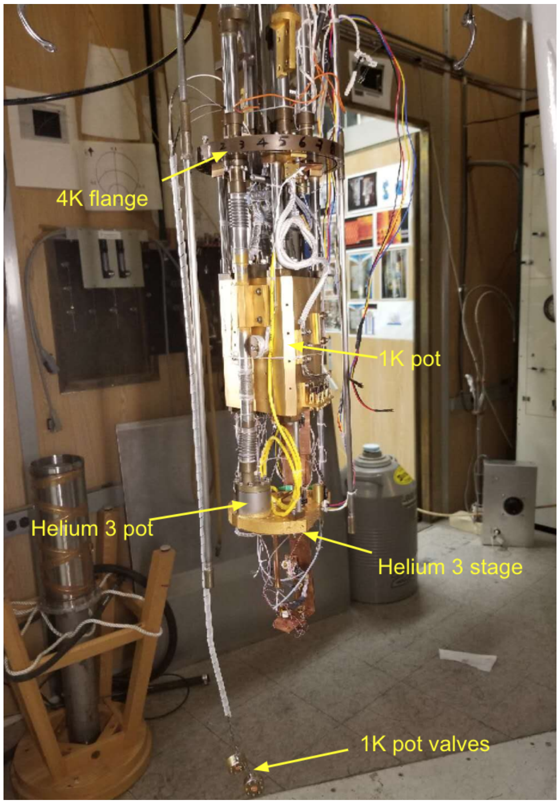

Figure 2.22: A picture of the tower in the vacuum can. Some important elements are labelled.

Resistor	C7415	C7379	Ge22726	Bath Resistor
Resistance (Ω)	8.8	8.07	1.24	472.5
^{3}He stage spear	1 K pot spear	Short Level Detector	Heater #1	Heater #2
271.7	533.1	475.6	467.1	355.0

Table 2.2: Resistances for some of the thermometers, level detectors and heaters at room temperature.

manium thermometer. Spear thermometers are auxiliary thermometers providing only approximate temperatures. Heaters are numbered according to the order of their jack-plug on the panel of the junction box from top to bottom. The resistance of heater #2 is much smaller than heater #1 because it is connected using heavier copper wires so that one can apply larger currents should more heat be required.

2. If the experiment requires a magnetic field, the magnet should be assembled and the resis-

tances of the different sections should be verified and recorded. During the operation of the magnet, a maximum current of $74\,\mathrm{A}$ can be applied. The nominal values of the resistances of the different sections are listed in table 2.3.

Section	Resistance (Ω)
Between V_+ and V_- (At the top of the cryostat)	20.7
Across the copper plate junction (In the middle of the cyostat)	0.00
The superconducting coil	20.7
The heater (At the bottom)	84.0

Table 2.3: Resistances of different sections of the magnet. Among them, the first three are measured using a four wire configuration. The last one is measured using a two wire configuration.

3. The quality of the vacuum within the vacuum can is critical for the STM experiments. If ^{4}He were to leak from the bath or the 1K pot to the vacuum can, the resulting superfluid ^{4}He can setup up an effective heat pipe by flowing from a cold section of the cryostat to a warmer section, evaporate into gas that can then flow to the cold section and recondense. Because the heats of vaporization and condensation are so large, this mechanism can easily prevent the cryostat from cooling below $2.3\,\mathrm{K}$.

   These are the necessary steps to make a good low temperature vacuum seal. A lead O-ring of the right length should be cleaned and wetted with some vacuum grease to seal the 4 K flange. When tightening the screws on the 4K flange, a sound of squeezing the lead O-ring should be heard. After the vacuum can is installed, the helium leak checker should be started and connected. Before raising the bath, ^{4}He should be sprayed around every flange and fitting from the top of the cryostat to the bottom of the vacuum can to make sure that there is no obvious leak. After the bath is raised, the space between the bath and the vacuum can should be pumped out and back filled with ^{4}He. The same procedure should also be done to the 1K pot. Plotting the leak level through the whole process can help identify very small leaks or diffusive leaks by establishing the background. Because the two inlet valves should be tested, and fixed if there is a problem, pumping the 1K pot should be done before the bath is raised. One can always pump the 1K pot again before transferring liquid nitrogen. When pumping on the pot with both valves closed, the pressure in the 1K pot should be able to reach $\sim 2 \times 10^{-2} Torr$. With the fast valve closed and the slow valve open, the pressure should be $\sim 4 \times 10^{-2} Torr$. With both valves open, it should be $\sim 2 \times 10^{-1} Torr$.

Before adding neon or hydrogen as an exchange gas between the cryostat inside the vacuum can and the bath, all the pipes of the gas panel should be pumped by a mechanical pump to avoid any contamination. After several cooldowns, because ^{4}He can diffuse through the fiber glass walls of the dewar, the internal vacuum of the dewar may become"soft" and thereby degrade the thermal insulation. This vacuum space should be pumped before liquid nitrogen is transferred.

2.6.2 Liquid Nitrogen Cooling

1. As one slowly transfers liquid nitrogen into the bath the bath resistance will gradually increase. Once the value reaches 553 ohms liquid nitrogen is accumulating at the bottom of the dewar. After the transfer completes (usually, $15 l$ to $20 l$ of liquid nitrogen is used), seal all openings from the bath to the external environment but one. This opening should be blocked by a rubber hose with a small cut slit. In this way, if the pressure in the bath is higher than the atmosphere, gas can come out. If it is slightly lower, the slit will close to prevent air from entering the bath.

2. In less than one day, the cryostat will cool down to a temperature close to 77 K. At this time check all the resistors, heaters and the sample again. The nominal resistances at 77 K are listed in Table 2.4.

   The next step is to push all of the liquid nitrogen out of the bath. In particular, we don't want any liquid nitrogen at the bottom when liquid helium is transferred because this will waste liquid helium. First, the exchange gas should be pumped out of the vacuum can. In this way, the tower inside will remain cold. Afterwards, clean high pressure nitrogen gas

Resistor	C7415	C7379	22726
Resistance (Ω)	14.7	13.7	1.68
Bath Resistor	^{3}He stage spear	1 K pot spear	Short Level Detector
550.7	617.6	308.6	426.14

Table 2.4: Resistances for some thermometers, level detectors and heaters at liquid nitrogen temperature.

should be pushed into the bath. A pressure of around 150 mbar should be enough to push the liquid nitrogen out through the transferring line. When no more liquid comes out and the pressure in the bath keeps dropping, most of the liquid nitrogen has been pushed out and there is only a small amount left at the bottom. To get that out, one repetitively pumps the bath to vacuum and backfills with room temperature nitrogen gas through the transfer stick so that the hot gas goes directly to the bottom of the dewar. By pumping the bath, the boiling point of the liquid nitrogen drops thus evaporating faster. As it evaporates, the liquid nitrogen may solidify. In each cycle, one backfills with nitrogen gas to warm up the bottom of the dewar and boil off more of the liquid nitrogen. After several cycles of pumping and backfilling, the change of the bath resistance will be less than 2 ohms indicating that the bath is completely dry. At this point one refills the bath with ^{4}He gas. During this process, one can reconnect the leak checker and plot the background level to make sure there is no leak. A leak can develop between room temperature and liquid nitrogen temperature because of the differential thermal contraction between parts of the flanges. If there is no leak, one should recheck the 1K pot inlet valves and backfill the 1 K pot with ^{4}He. Again the leak checker is monitored to make sure there is no leak from the 1 K pot.

2.6.3 Liquid Helium Cooling

1. Before transferring liquid helium, the transfer stick should be pumped out to make sure it has not been contaminated with ^{4}He gas. For the first transfer, the transfer stick should be inserted into the transfer extension that reaches the bottom of the dewar so that the helium gas/liquid will be pushed to the bottom of the bath. For later transfers, the transfer stick

should sit above the extension so that the liquid helium will come out above the 4K flange. Otherwise, the initial flow of hot gas would be injected into the liquid helium at the bottom of the bath and boil away some of the liquid and cause turbulence. To ensure that the two halves of the transfer stick are sufficiently precooled, one should see dense white clouds coming out of them before connecting them,

2. Use high pressure ^{4}He gas to push the liquid helium out of the dewar. When the bath cools below the temperature of liquid nitrogen, add heat exchange gas (neon or hydrogen) into the vacuum can. Monitor the bath resistance during the cooldown to make sure it does not exceed 690 ohms. Otherwise, the exchange gas will freeze out and it will take forever to cool down the tower. A flow rate of 8 on the flow meter is a reasonable speed to feed in the ^{4}He gas. The exchange gas can be pumped out when the ^{3}He stage reaches around 22K if neon is used, and around 11K if hydrogen is used. After the exchange gas is pumped out, one can increase the flow rate of ^{4}He to actually push liquid helium into the bath until it reaches the top of the level detector. At this point one can open the fast 1K pot inlet and start pumping on the pot. After ten minutes or so, close the fast valve and open the slow valve. The tower should soon reach a temperature below 2K. If necessary, another leak check can be performed.

3. To use the ^{3}He system, the liquid nitrogen trap should be prepared. Turn on the cooling water circulation system. Open the valves from the ^{3}He tank to the ^{3}He pot on the ^{3}He stage to allow ^{3}He to be liquified and drip into the pot. Close the valve from the tank to the exhaust of the backing pump. Turn on the backing pump and then the roots blower. At this time ^{3}He gas should be circulated in the system. When the vacuum pressure measured at the mouth of the roots blower reaches around $9 \times 10^{-3} Torr$, there should be enough ^{3}He liquified in the pot for continuous operation. The ^{3}He stage will soon be cooled down to a temperature below 1 K.

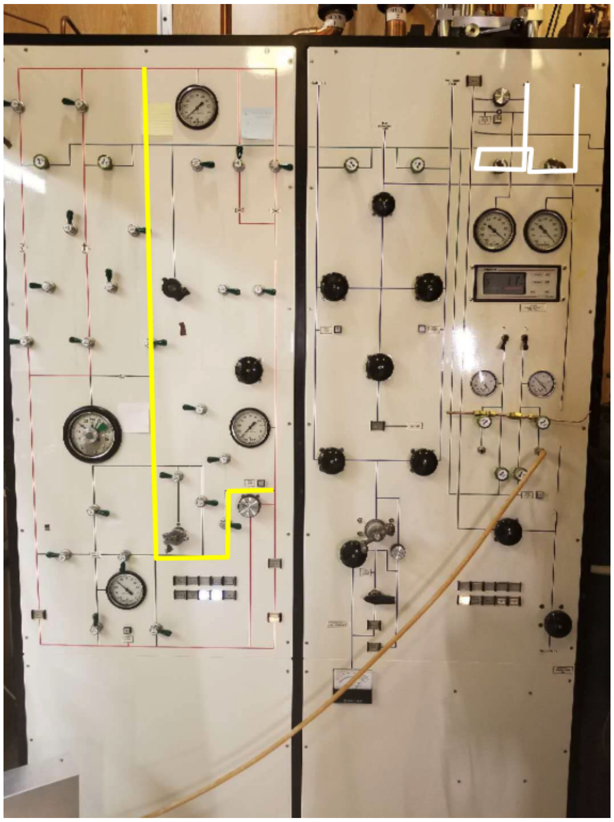

Figure 2.23: The main and the ^{3}He panels. The white and yellow lines show the two paths mentioned in the text.

2.6.4 Warm Up

1. The main concern during warmup is the expansion of gas. The valve from the bath to the ^{4}He recovery line should be open. The four valves that control the two 1K pot inlets should be open. In case that these valves are blocked by ice or dust, the 1K pot can be connected to the bath through a path on the main panel which is highlighted by the white line in Fig. 2.23. The volume on the condensing side of the ^{3}He pot on the ^{3}He circulating system is very small and should be connected to the pumping line before the roots blower. This can be accomplished through the path shown by the yellow line in Fig. 2.23.
2. After the tower warms up to a temperature above 77 K, hot nitrogen gas can be blown into the bath to speed up the process.

3. CHARACTERIZATION OF HFNISN

3.1 Background Knowledge

Full-Heusler compounds belong to the Fm-3m space group. Their crystal structure can be treated as four interpenetrating face-centered cubic (FCC) sublattices. Inside the corresponding half-Heusler compounds, one of the FCC lattices is replaced by vacancies. Due to this singular crystal structure, these materials can have intrinsic disorder. Taking ZrNiSn as an example, its properties and in particular the resistivity can be dramatically changed by annealing. Early computer simulations of the X-ray diffraction (XRD) results [27] support a substitution between the Zr and Sn atoms. However recently, there is contradictory evidence from the refinement of the XRD and electron micro probe analyzer (EPMA) results [28] that support the idea that interstitial Ni atoms can partially occupy the vacancy sites. Enthalpy calculation using a density functional theory (DFT) approach supports the same argument [29]. Given the symmetry between the Ni and the vacancy sites, such substitution would be more intuitive.

While full-Heusler compounds are all metals, half-Heusler compounds with 18 valence electrons are unusual. They are either semimetals or semiconductors. Localization of electrons is observed in many experiments [30, 27] including Raman spectroscopy, infrared spectroscopy, resistivity etc. Many characteristics of the half-Heusler are abnormal: (1) Similar to the heavy fermion materials, the heat capacity at low temperature depends linearly on the temperature, (2) The resistivity shows a crossover from an exponential semiconductor behavior at high temperatures to a variable range hopping behavior at low temperatures. (3) Infrared (IR) spectroscopy indicates a pseudo-gap instead of a true gap. (4) Measurements of the Hall effect show that the sign of the carriers are negative across the whole measured temperature range. Consequently, the assumpion of a simple semiconductor gap is insufficient to explain all these phenomena.

A narrow valence band originating from the vacancy lattice is proposed. The band overlaps with the conduction band forming a pseudo-gap. From the IR spectroscopy, the states in the pseudo-gap increase as temperature increases and is explained by the self trapping between potential wells [31].

Half-Heusler materials are potential thermoelectric materials. According to the formula for the thermoelectric figure of merit (ZT), $ZT = \frac{\sigma S^2}{\kappa} T$, a larger electric conductivity and a smaller thermal conductivity lead to a better heat conversion efficiency. Half-Heusler compounds have a very good balance between the electric and thermal conductivity. Moreover, multiple methods can be used to engineer the properties of half-Heusler materials. For example, doping can change their electron structures or their chemical potentials. Microstructures like grain boundaries can be introduced to influence the transport of both electrons and phonons.

The intrinsic disorders play a very important role in the properties of half-Heusler materials. After half a century of research, disordered systems still hold many mysteries. Ideal materials are periodic Bravais lattices. With increasing disorder, the diffusion of electrons will be impeded, leading to either weak localization or weak anti-localization (WAL) and eventually to Anderson localization. Because disorder can breakdown momentum conservation, they can also enhance the Coulomb interaction and create another kind of gapped states as in Mott localization. Systems with both disorder and strong Coulomb interactions serve as attractive models for both theorists and experimentalists. The combination of the randomness of the disorder and the multi-body nature of the Coulomb interaction can pose many technical difficulties.

At low temperatures, compounds with WAL show a variable range hopping (VRH) resistivity. Mott gave the initial formula:

$$\sigma \propto exp[-(\frac{T_0}{T})^{1/4}] \tag{3.1}$$

However, A. L. Efros et al. [32] suggest that the vanishing density of states because of the Coulomb gap due to the Mott transition will lead to a faster drop of the conductivity versus the temperature.

$$\sigma \propto exp[-(\frac{T_0}{T})^{1/2}] \tag{3.2}$$

Experimentally, exponents of 1/2, 1/3 and 1/4 have all been observed.

A good comprehensive book about disordered metals was written by A. L. Efros et al [33]. Formulas of resistivity, density of states, the Hall effect and many other properties are all deduced. For each property, the influence of dimensionality is also discussed. Because the book was published in the 1980s, some of its views may be out of date but most of his conclusions are still used as references in the study of disordered systems.

3.2 Experimental Details

Sample growth and quality tests, details for resistivity and magnetoresistance measurements are described in the paper of our colleague [1]. The samples are single crystals grown using a flux method. Tin is used as the solvent. A saturated solution is slowly cooled down to allow the precipitation of the solute. The process either starts from the self-nucleation of the solute or is triggered by some seed. The crystals produced are usually smaller than 1 mm.

STS spectra are measured using our low temperature STM mounted on the ^{3}He cryostat. The STM's ability to obtain images with atomic resolution was demonstrated on graphite and self-assembled dodencanethiol monolayer on gold surface. Mechanically cut platinum-iridium tips were used. Because of a lack of in-situ tip treatment device, the tips were annealed using a Bunsen flame [34] in order to get reproducible spectra. Using the same type of tips, no ZBA were observed in the spectra of gold down to 77 K. Samples were broken right before experiments to expose fresh surfaces. Differential conductances were measured by a standard lock-in technique with a 0.5 mV modulation.

3.3 Results and Discussion

3.3.1 Temperature dependence of resistivity

To illustrate the strongly disordered character of HfNiSn consider that at 10 K, the resistivity of our samples varies from 0.06 Ωcm to 0.5 Ωcm. The corresponding carrier concentration ranges from $2.8 \times 10^{17} cm^{-3}$ to $3.1 \times 10^{18} cm^{-3}$. Using the smallest resistivity and the largest carrier concentration, the diffusion coefficient $D = \frac{k_B T}{\rho n e^2}$ is estimated to be 0.029 cm^2/s. Choosing a

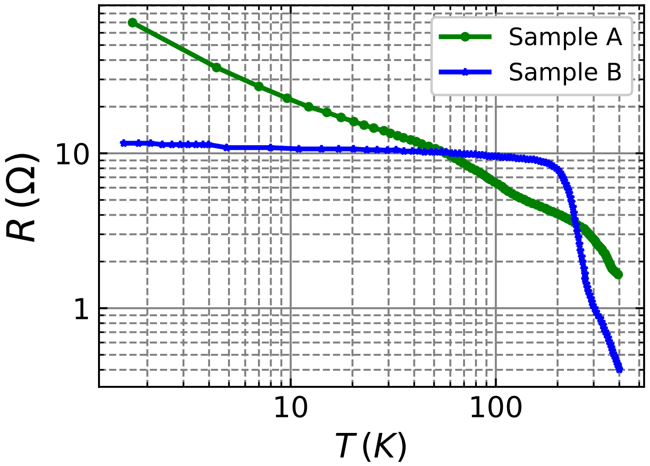

Figure 3.1: Temperature dependence of the resistance of two samples. Sample A shows the VRH behavior at low temperatures whereas Sample B saturates at low temperatures.

median reported effective mass $m^* = 2m_e$, we can then calculate the dimensionless parameter that is commonly used to evaluate the degree of disorder, $k_F l_e \approx \frac{3Dm^*}{\hbar}$ to be ≈ 0.15. A value much less than 1 indicates strong disorder. To confirm our estimate, a calculation using the resistivity and the carrier concentration of ZrNiSn in Ref. [27] gives a similar value.

The typical resistance of HfNiSn obeys VRH at low temperature [27, 35]. Some of our samples, such as sample A in Fig. 3.1 show the same kind of behavior. The resistance of sample A is plotted versus $T^{-1/4}$ in Fig. 3.2. The straight curve below 48 K confirms the expression $\rho = \rho_0 exp[(\frac{T_0}{T})^{1/4}]$. The 1/4 exponent is different from the 1/2 proposed by Mott may be due to the fact that our ZBA is a pseudogap. Therefore, even at $0\,\mathrm{K}$, there are plenty of states at the Fermi energy.

We also have some samples, such as sample B in Fig. 3.1, that show a resistance that saturates below around $200\,\mathrm{K}$. Our colleague interprets that this is a result of topological edge states and is trying to find strong evidence in support of this interpretation [1]. In the framework of disorder, we refer to the observation of Yu et al. [36]. The resistance of a hopping system can be independent of temperature at high electric fields, i.e. $E > E_0 = W/(ed)$, where W is the Coulomb barrier and d is the distance between nearest neighbors (NN). With the help of the electric field, hopping between NN are favored again instead of variable range hopping. Samples like sample B may have

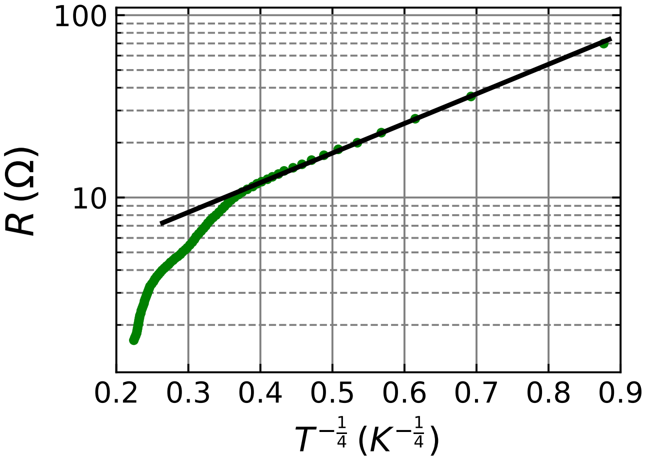

Figure 3.2: Resistance of sample A versus $T^{-1/4}$. Resistance data are provided by our colleague [1].

very small W and large d leading to a small E_0 of just thousands of V/m.

3.3.2 Local density of states

Figures 3.3b and 3.3c show a scanning electron microscope (SEM) and an STM image of a freshly broken HfNiSn surface respectively. The flat surface seen by SEM looks cratered in the STM image. Because STM measures the local density of states, the nanometer scale roughness provides us some insight into how localized the electronic wave functions are.

Figure 3.4a shows the normalized tunneling conductance at different temperatures. Although the spectra may change slightly across the surface, the main features remain the same. The inset shows the spectra at 13 K and 290 K over a larger bias range. We can clearly see that the ZBA has a V^α dependence with a minimum around $-7mV$. Commonly observed in disordered systems and theoretically studied by Altshuler and Aronov [37] and McMillan [38], this type of ZBA is believed to be a consequence of localization and Coulomb interaction.

One way to verify these spectra is to plot $\frac{G[V,T]-G[0,T]}{\sqrt{T}}$ versus $\sqrt{\frac{eV}{k_BT}}$. Spectra of different temperatures should then collapse onto a universal scaling curve. Our spectra roughly follow this scaling law. However, after a more careful normalization by overlapping the spectra at high bias indicates that a scaling of $(G[V,T]-G[0,T])/T^{0.3}$ versus $(eV/k_BT)^{0.3}$ generates a perfect fit.

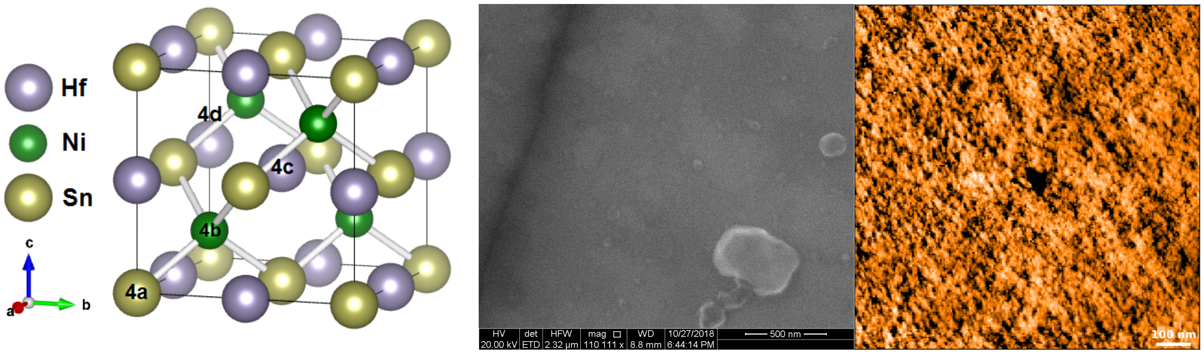

(a) (b) (c)

Figure 3.3: (a) Crystal structure of HfNiSn. 4 Wyckoff positions are labelled. The 4d position is occupied by vacancies. (b) SEM image of a freshly broken surface. (c) STM image of the same surface.

This is shown in Fig. 3.4b. The scaling of $(G[V,T] - G[0,T])/T^{0.3}$ versus $(eV/k_BT)^{0.3}$ was also observed in measurements of copper nanoconstrictions [39]. The V^{α} behavior also suggests that the spectra are from 3D bulk states, because a log dependence would be expected in the 2 dimensional case [40, 33].

Two level systems (TLSs) is another possible explanation for this kind of ZBA [39, 41, 42]. TLS is an analog to the two channel Kondo effect in which electrons are scattered by atoms or atom groups that can tunnel between two states. Applying the TLS model to HfNiSn is reasonable because of existence of the vacancy lattice in HfNiSn and the symmetry between these vacancies and the 4b nickel sites. On the other hand, this explanation may not apply because it would mean that the nonmagnetic Kondo temperature T_k woluld expected to be less than a few Kelvin [43].

The appearance of a ZBA automatically solves some of the confusion about early experimental results. In order to explain the absence of a finite band edge in the infrared absorption spectra and the crossover of the resistance from a semiconductor behavior to a VRH behavior, Aliev et al. [27] proposed a narrow band generated by the vacancy lattice which overlaps with the conduction band. But the absence of a finite band edge is apparent because the ZBA is a pseudogap. Aliev also explains the temperature dependence of the gap as a consequence of the temperature dependence of self-trapping between potential wells, whereas the ZBA gets shallower because of thermal fluc-

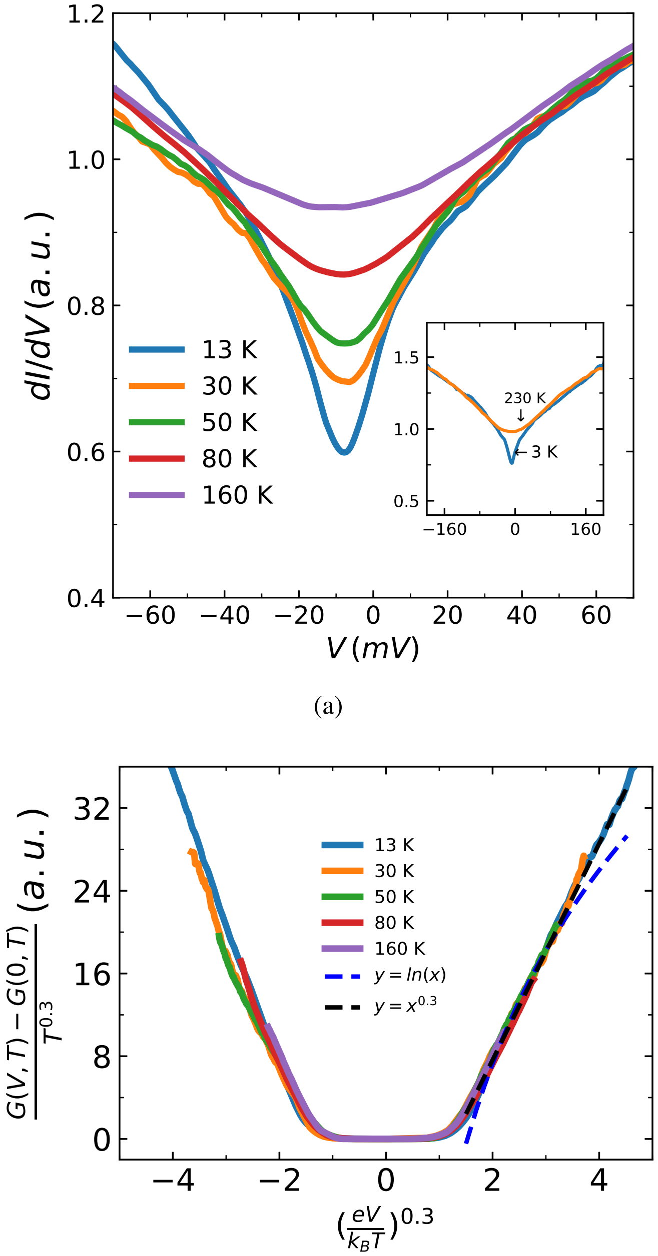

(a)

(b)

Figure 3.4: (a) LDOS of a single crystal HfNiSn from 13 K to 160 K. Spectra are normalized by overlapping their values at high positive bias voltages. Inset shows spectra at 13 K and 290 K over a larger bias range. (b) Plot of $(G[V,T]-G[0,T])/T^{0.3}$ versus $(eV/k_BT)^{0.3}$. All spectra between 13 K and 160 K collapse to a universal curve. The black and blue dashed lines are the best fit supposing $G[V,T]$ is proportional to $V^{0.3}$ or $ln[V]$ respectively.

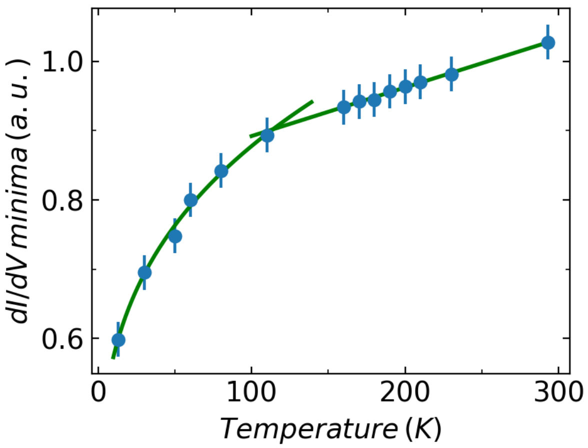

Figure 3.5: The minima of the spectra versus temperature. There is a $T^{0.3}$ power law behavior at low temperature and a linear behavior at high temperature.

tuation [44]. For the half-Heusler materials with 18 valence electrons, there is a paradox that the smaller the resistivity at low temperature, the larger the energy gap [45]. This can be understood if the intrinsic disorder is donors on the one hand and cause localization on the other.

Mathematically, there are two more interesting coincidences extracted from the LDOS. Firstly, the minima of the spectra show a crossover from a $T^{0.3}$ behavior to a linear behavior at around 120 K, as shown by Fig. 3.5. On the basis of the theory by Altshuler and Aronov [37], we believe that this crossover is caused by the mean free path of the electrons dropping below their wavelength as the temperature increases. Interestingly, 120 K is about the temperature at which the resistances of some samples start to saturate. The crossover of resistance from a VRH behavior to a semiconductor behavior is typical in disordered semiconductors [46, 47]. Further experiments to confirm the correlation between the crossover of the ZBA and the crossover of the resistance by performing measurements on samples with distinct crossover temperatures would be very interesting.

Secondly, from the Bardeen's formula, we know that the tunneling current of an STM is a convolution between the occupied tip states and the unoccupied sample states when a negative bias is applied on the sample. If we further suppose that the tip has a constant LDOS, the tunneling conductance will be simplified to a convolution between the sample states and the derivative of the

Fermi distribution.

$$\left.\frac{dI}{dV}\right|_{V=\frac{\epsilon_0}{e}} = \int_{-\infty}^{\infty} s[\epsilon]\frac{\partial f[\epsilon-\epsilon_0]}{\partial \epsilon}d\epsilon \tag{3.3}$$

Where $s(\epsilon)$ is the LDOS of the sample. $f[\epsilon-\epsilon_0]$ is the Fermi distribution. Because at $0\,\mathrm{K}$, the derivative of the Fermi distribution is a delta function, $\frac{dI}{dV}$ reproduces the sample LDOS. As the temperature increases, the half width of the derivative of the Fermi distribution increases and the tunneling conductance will become smoother.

In the simplest case of an electron gas, the Fermi distribution is a sigmoid function given by

$$f(\epsilon) = \frac{1}{e^{(\epsilon-\epsilon_0)/k_BT}+1} \tag{3.4}$$

where k_B is the Boltzmann constant, ϵ_0 is the chemical potential.

In reality, this is unlikely to be the true distribution in the presence of a strong Coulomb interaction between electrons or scattering by localized magnetic impurities. Surprisingly, the measured tunneling currents at different temperatures can all be reproduced using a Fermi distribution of

$$f(\epsilon) = \frac{1}{e^{3(\epsilon-\epsilon_0)/2k_BT}+1} \tag{3.5}$$

and a square root LDOS at $0\,\mathrm{K}$. Here, we show this simple convolution also satisfies the universal scaling rule, that when $\frac{G[V,T]-G[0,T]}{\sqrt{T}}$ is plotted versus $\sqrt{V}$, curves at different temperatures coincide.

We suppose the LDOS of the sample at $0\,\mathrm{K}$ is

$$s(\epsilon) = \begin{cases} a\sqrt{-\epsilon}+b & \epsilon \le 0 \\ a\sqrt{\epsilon}+b & \epsilon > 0 \end{cases} \tag{3.6}$$

Where a, b are two constants. Then at finite temperatures, the tunneling conductance becomes

$$\begin{aligned}\frac{dI}{dV}\Big|_{V=\frac{\epsilon_0}{e}} &= \int_{-\infty}^{0} \frac{(a\sqrt{-\epsilon}+b)e^{3(\epsilon-\epsilon_0)/2k_BT}}{(e^{3(\epsilon-\epsilon_0)/2k_BT}+1)^2} \times \frac{3}{2k_BT} d\epsilon \\ &+ \int_{0}^{\infty} \frac{(a\sqrt{\epsilon}+b)e^{3(\epsilon-\epsilon_0)/2k_BT}}{(e^{3(\epsilon-\epsilon_0)/2k_BT}+1)^2} \times \frac{3}{2k_BT} d\epsilon\end{aligned} \tag{3.7}$$

Replacing ϵ by $\epsilon' = \frac{\epsilon}{k_BT}$, we obtain

$$\begin{aligned}\frac{dI}{dV}\Big|_{V=\frac{\epsilon_0}{e}} &= \frac{3}{2}\sqrt{k_BT} \int_{-\infty}^{0} \frac{(a\sqrt{-\epsilon'}+b)e^{\epsilon'-3\epsilon_0/2k_BT}}{(e^{\epsilon'-3\epsilon_0/2k_BT}+1)^2} d\epsilon' \\ &+ \frac{3}{2}\sqrt{k_BT} \int_{0}^{\infty} \frac{(a\sqrt{\epsilon'}+b)e^{\epsilon'-3\epsilon_0/2k_BT}}{(e^{\epsilon'-3\epsilon_0/2k_BT}+1)^2} d\epsilon'\end{aligned} \tag{3.8}$$

It is clear that

$$\frac{dI}{dV}\Big|_{V=\frac{\epsilon_0}{e}} \times \frac{1}{\sqrt{T}} = f[\sqrt{\frac{\epsilon_0}{T}}] \tag{3.9}$$

Figure 3.6 shows the tunneling conductance from 13K to 80K. The blue lines are the analytical curves, and the green lines are the experimental results. The fits are almost perfect, especially at $80\,\mathrm{K}$ and the fits at positive bias are better than at negative bias. This supports the viewpoint that the positive half of the tunneling conductance is dominated by the sample states and the negative half is dominated by the tip states.

We have also observed a shift of the LDOS minima in a magnetic field. This phenomenon is not consistent and only appears on two samples. For one sample, when the magnetic field reaches above $0.6\,\mathrm{T}$, the minimum shifts from -7mV to -1.5mV. For another sample, there is a tiny shift from -7.5mV to -7mV at a magnetic field of 0.4T. Although HfNiSn is a diamagnetic material, the susceptibility shows a paramagnetic signal at small fields. This paramagnetic signal may be cause by some paramagnetic impurities. They may also be the reason for the shift. If the shift is truly caused by scattering from localized spins, doping the sample with magnetic elements may enhance it. Another possibility is that the shift depends on the angle between the magnetic field and certain

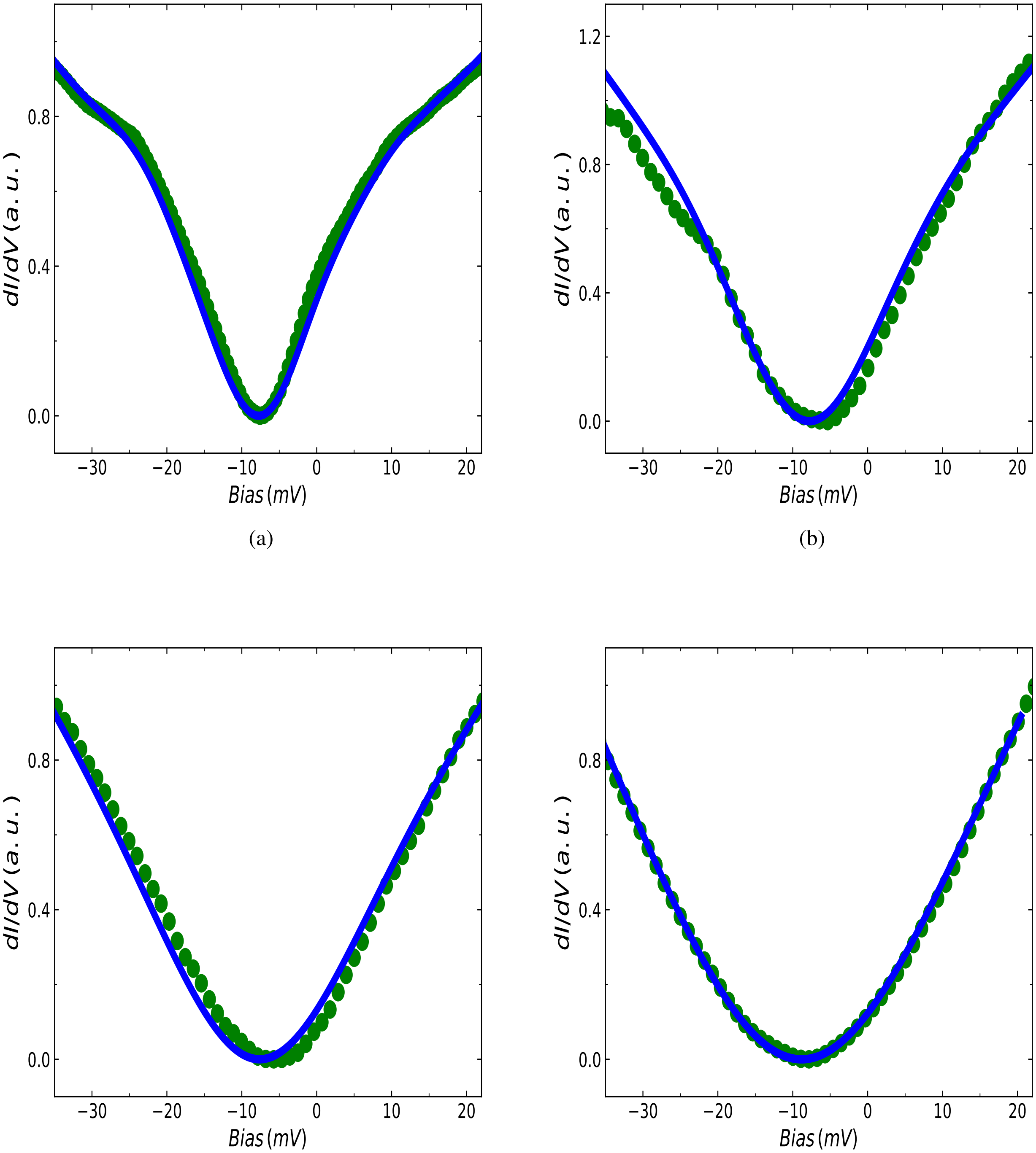

(a)

(b)

(c)

(d)

Figure 3.6: (a) through (d) are the tunneling conductance at 13K, 30K, 50K and 80K. The green dots are the experimental data. The blue curves are obtained from numerical solutions of Eq. 3.8.

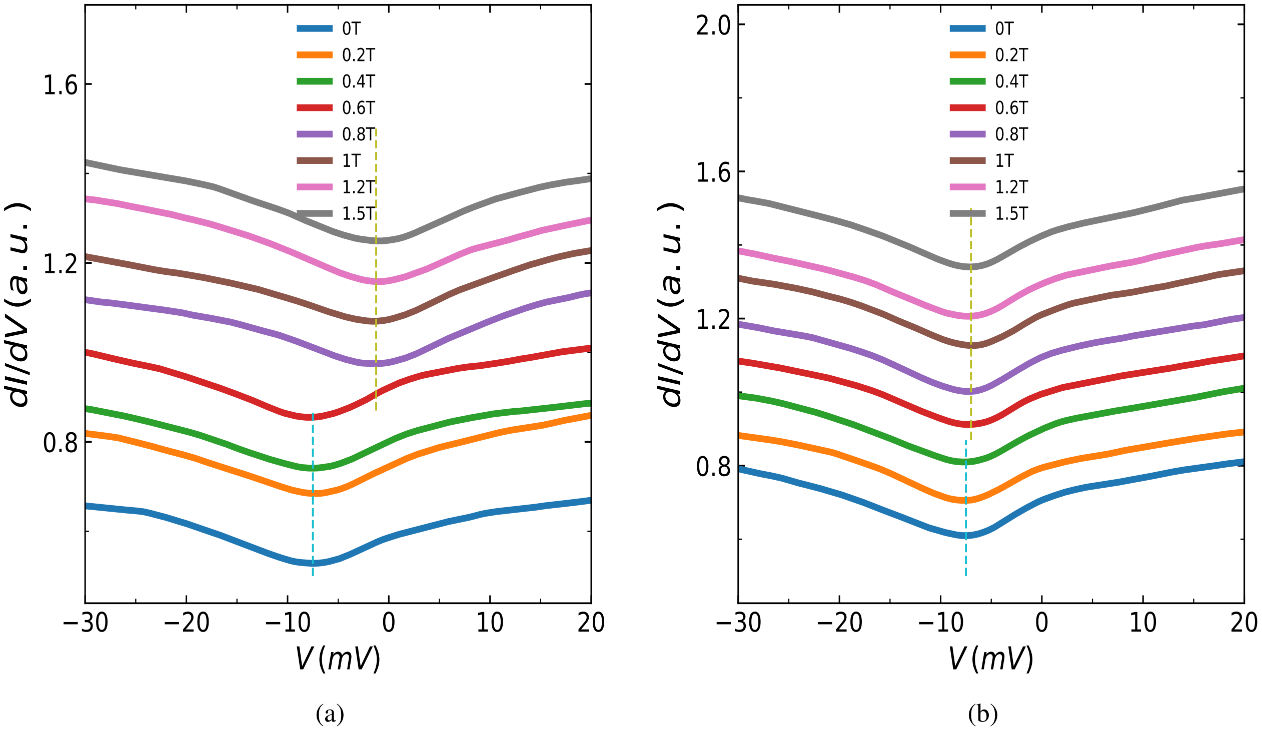

(a) (b)

Figure 3.7: Shift of the LDOS minima in a magnetic field. (a) The sample shows an obvious shift of 5mV. (b) The sample shows a tiny shift of 0.5mV.

crystal orientation.

For a magnetic Kondo material in the presence of a magnetic field, the potential wells of local spins become asymmetric. The Zeeman term will split the original peak or valley in the LDOS into two depending on whether it is the one-channel or two-channel Kondo effect. The separation of the two peaks or valleys will be proportional to the field. In a two level system, a magnetic field will break the spin up and down degeneracy of the electrons. This will make the two channels anisotropic. The result is that the magnitude of the minima of the LDOS should be proportional to the field at temperatures close to zero. We do not observe either of these cases.

3.3.3 Magnetoresistance

The magnetoresistance of a single crystal HfNiSn and some other half-Heusler compounds are previously discussed by Ahilan et al. [35]. The data provided by our collaborator is very consistent with this published data. However, in their discussion, the role of disorders is ruled out simply because the sample is a single crystal. Here, we show that the magnetoresistance is clearly a result of localization.

WAL is a quantum conduction phenomenon occurring in disordered systems. With the presence of a strong spin-orbit coupling or a π Berry's phase, interference between currents traveling in opposite directions in a self-intersecting loop becomes constructive. When a magnetic field is applied, another phase is added to the carriers and the WAL effect is reduced, resulting in an increasing resistance. This effect on the magnetoresistance should follow a B^2 behavior at low fields and a $\sqrt{B}$ or a less precipitous behavior at high fields. As the temperature increases, the range of the B^2 region should expand to higher field. Plotting our data versus B^2 in Fig. 3.8(b) and $\sqrt{B}$ in Fig. 3.8(c) illustrate these characteristics.

The formula for 3D WAL is provided by Fukuyama and Hoshino (F-H) [48, 49, 50].

$$\frac{\Delta\rho_{WAL}[B]}{\rho[0]^2} = \frac{e^2}{2\pi^2 h}\sqrt{\frac{2\pi eB}{h}}\left(\frac{1}{2}f_3[\frac{B}{B_\phi}] - \frac{3}{2}f_3[\frac{B}{B_2}]\right) \tag{3.10}$$

Where $B_\phi = B_i + 2B_S$ and $B_2 = B_i + \frac{2}{3}B_S + \frac{4}{3}B_{SO}$, B_i, B_S and B_{SO} stands for the characteristic fields for inelastic, spin-flip and spin-orbit scattering respectively. f_3 is an infinite series,

$$f_3[y] = \sum_0^\infty \left(2(n+1+\frac{1}{y})^{\frac{1}{2}} - 2(n+\frac{1}{y})^{\frac{1}{2}} - (n+\frac{1}{2}+\frac{1}{y})^{-\frac{1}{2}}\right) \tag{3.11}$$

Depending on the materials, extra components are added, e.g. the Maki-Thompson term for superconductors [51], the Stoner enhancement factor for paramagnetic materials [52], and the electron-electron interaction terms for systems with large Coulomb interaction (CI) [50]. The F-H model works qualitatively, but many analyses show clear deviations from the model, e.g. agreement only at low fields or a tendency to fail at low temperature [50, 53, 54, 55]. Therefore, we fit

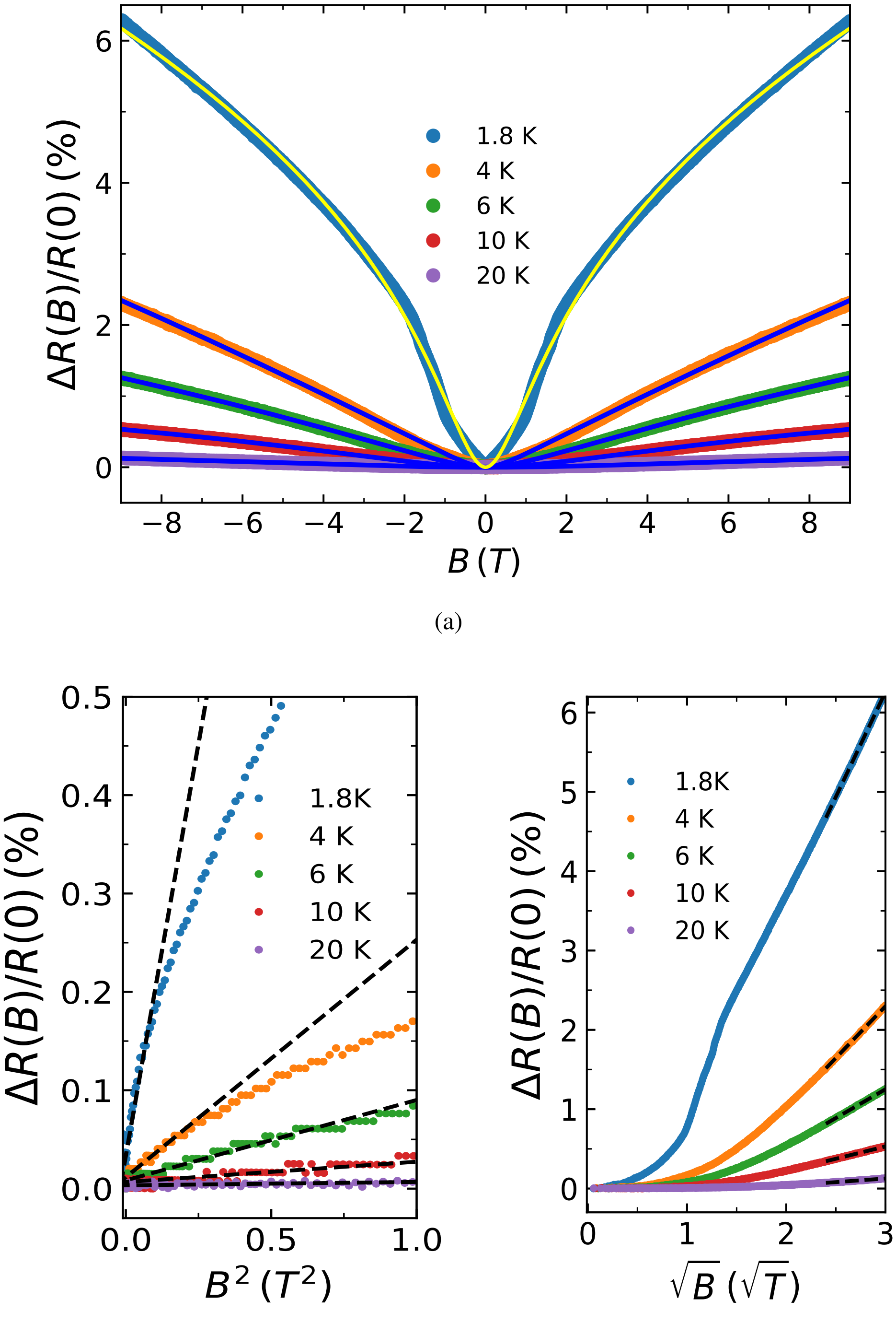

(a)

(b)

(c)

Figure 3.8: (a) Magnetoresistance $\Delta R/R = (R[B] - R[B=0])/R[B=0]$ of a single crystal HfNiSn at different temperatures. The thin blue curves are the best fits generated using a sum of the F-H model and the orbital correction due to electron-electron interaction. The thin yellow curve is generated using the same empirical formula mentioned by Rosenbaum et al. [17]. (b) Magnetoresistance versus B^2. Dashed lines are linear fits. (c) Magnetoresistance versus $\sqrt{B}$. Magnetoresistance data are provided by our collaborator. [1]

the model to our data mainly to demonstrate that our result is similar to the typical magnetoresistance of disordered systems.

Because our samples have low diffusion coefficients, the complete F-H model is used instead of the simplified Kawabata model and the spin-flip scattering by magnetic impurities is ignored. The diffusion-channel term of CI is added as suggested by the ZBA.

$$(\frac{\Delta\rho}{\rho^2})_{DC} = \frac{e^2}{2\pi^2\hbar}\sqrt{\frac{eB}{\hbar}}\frac{F_\sigma}{2\sqrt{\pi}}(\frac{\pi k_B T}{2DeB})^{1/2} g_3[\frac{g\mu_B B}{k_B T}] \tag{3.12}$$

Where DC stands for the diffusion channel.

$$F_\sigma = -\frac{32}{3F}(1+\frac{3F}{4}-(1+\frac{F}{2})^{3/2})$$

$$F = \frac{\int d\Omega\, V[q = 2k_F sin(\theta/2)]}{\int d\Omega\ \ V[q=0]} \tag{3.13}$$

$$g_3[x] = \int_0^\infty d\omega\,(\frac{d^2}{d\omega^2}(\frac{\omega}{e^\omega - 1}))(\sqrt{\omega+x}+\sqrt{|\omega - x|}-2\sqrt{\omega})$$

V in the formula of F is the Fourier transform of the Coulomb potential. Therefore, F stands for the angular average of the interaction around the Fermi surface.

The entire formula for the magnetoresistance is a sum of Eqs. 2.1 and 2.9 in Ref. [49]. Relatively good fits are generated for curves above 1.8 K which are shown by the thin blue curves in Fig. 3.8a. From these fits, we can extract some parameters, especially the three characteristic fields. The green curve in Fig. 3.9 is a log-log plot of the dephasing fields $B_\phi = B_i + 2B_S$ versus temperature, the slope of which is 1.51. The B_{SO} is approximately a constant around $4.1\,\mathrm{T}$ and is much larger than the B_i as expected. F, the angular average of the screened Coulomb potential over the Fermi surface, is around 0.17, satisfying the condition that $0 \leq F \leq 1$. However, the curve at 1.8 K is different from others by a sharper turn from the B^2 region to the $\sqrt{B}$ region and a good

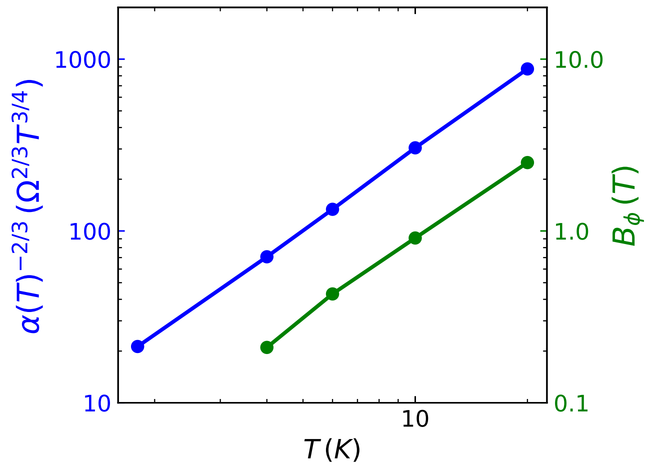

Figure 3.9: Loglog plot of $\alpha[T]^{-2/3}$ (left) and B_ϕ (right) versus temperature.

fit cannot be generated. However, this curve resembles the one of Si:P and the thin yellow curve in Fig. 3.8(a) is generated using the same empirical equation $\Delta\rho/\rho^2 = [1/(CH^2) + 1/(EH^{1/2})]^{-1}$ mentioned by Rosenbaum et al. [17].

There is a cleaner way to get the temperature dependence of B_ϕ. At low fields, the diffusion-channel term of CI is very small compared to the F-H term. In the limit of $B \to 0$, we also have $\gamma \to 0$ and $B \ll B_i \ll B_{SO}$. Because B_S is ignored, the F-H model becomes $\Delta\rho/\rho^2 \sim B^2/B_\phi^{3/2}$. Therefore, the temperature dependence of the coefficient $\alpha[T]$ of the low field approximate curve $\Delta\rho/\rho^2 \sim \alpha[T]B^2$ gives one the temperature dependence of B_ϕ.

$$\alpha[T] \sim B_\phi^{-\frac{3}{2}} \tag{3.14}$$

The blue curve in Fig. 3.9 is a log-log plot of $\alpha[T]^{-2/3}$ versus T. The slope is 1.54 which is very close to the value we get from the fitting parameter B_ϕ. Therefore, B_ϕ is obviously proportional to $T^{3/2}$.

It has been a convention to suppose that $B_\phi = B_i \sim \frac{1}{\tau_i} = \frac{1}{\tau_{ep}} + \frac{1}{\tau_{ee}}$. It is known that in a disordered system, the relaxation time for electron-phonon interactions should scale with temperature as $\tau_{ep} \sim T^{-p}$, where p can be 2, 3 or 4 [55, 56] and that for electron-electron interactions should scale as $\tau_{ee} \sim T^{-d/2}$, where d is the dimension of the system. Therefore, in HfNiSn, we believe that electron-electron scattering is dominant at low temperatures which is consistent with the implication of the ZBA.

Ahilan et al. observed a moderate linear magnetoresistance for polycrystalline HfNiSn. There are two common explanations for a linear magnetoresistance in amorphous semiconductors. The first one attributes the behavior to fluctuations of the electron mobility μ and the linear coefficient is then proportional to the standard deviation $< \mu >$. The second one is more classical. When the electrons are weakly localized, there will be paths perpendicular to the direction along the voltage drop adding Hall signal to the measured voltage. Therefore, the observation of the linear magnetoresistance is another evidence that HfNiSn resembles a disordered system.

3.3.4 LDOS of Other Half-Heusler Compounds

Figure 3.10 shows the LDOS of three other half-Heusler compounds besides HfNiSn. From left to right, it appears that a gap is opening. Interestingly, except for ZrCoPb which has a metal like constant LDOS, the others all obey perfect power laws with exponents 0.3, 1 and 2.1. The linear LDOS is especially confusing because traditionally only a linear dispersion relation in a 2 dimensional material can result in a linear LDOS. All these results were verified on at least two different samples. It also seems that the form of the LDOS does not depend on the density of disorders because we have measured both a good NbFeSb and a flawed NbFeSb sample.

The different LDOS should also be reflected in their electric properties. Figure 3.11 shows the resistivity of the four materials from the references indicated. As the temperature decreases, the resistivity of HfNiSn increases rapidly and saturates at around 200K as previously mentioned in Fig. 3.1. The resistivity of ZrCoSb increases moderately above 400K and decreases also moderately below 400K. NbFeSb has a relatively constant resistivity from 50 to 300K but increases exponentially below 50K. ZrNiPb has the smallest resistivity among the four materials and, with a little doping, can be easily changed from a semiconductor to a metal.

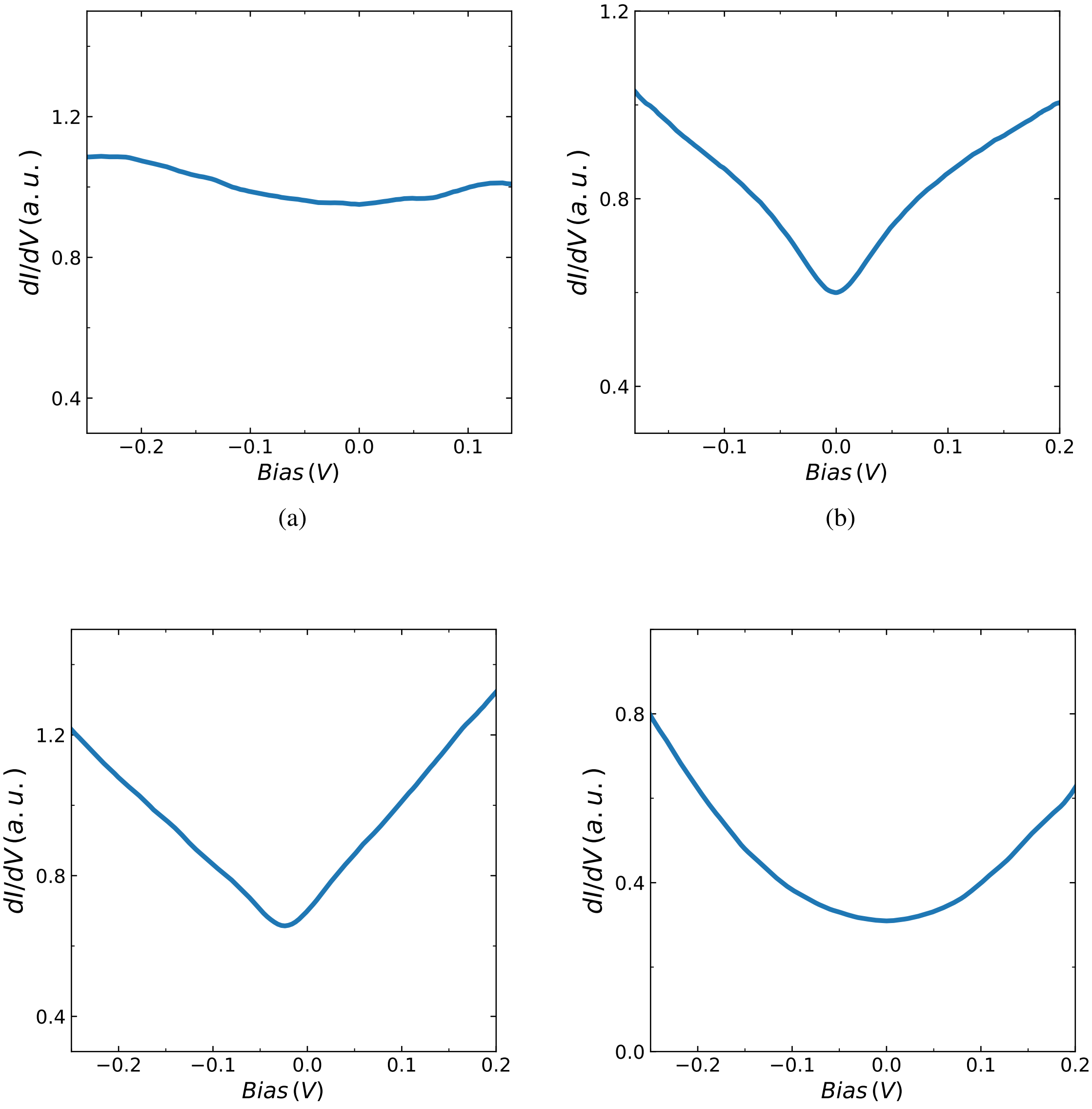

(a) (b)

(c) (d)

Figure 3.10: LDOS of four half-Heusler compounds with 18 valence electrons. (a) ZrNiPb. (b) HfNiSn. (c) ZrCoSb. (d) NbFeSb. The samples of ZrNiPb, ZrCoSb and NbFeSb are provided by Fei Tian of Dr. Zhifeng Ren's group of the University of Houston.

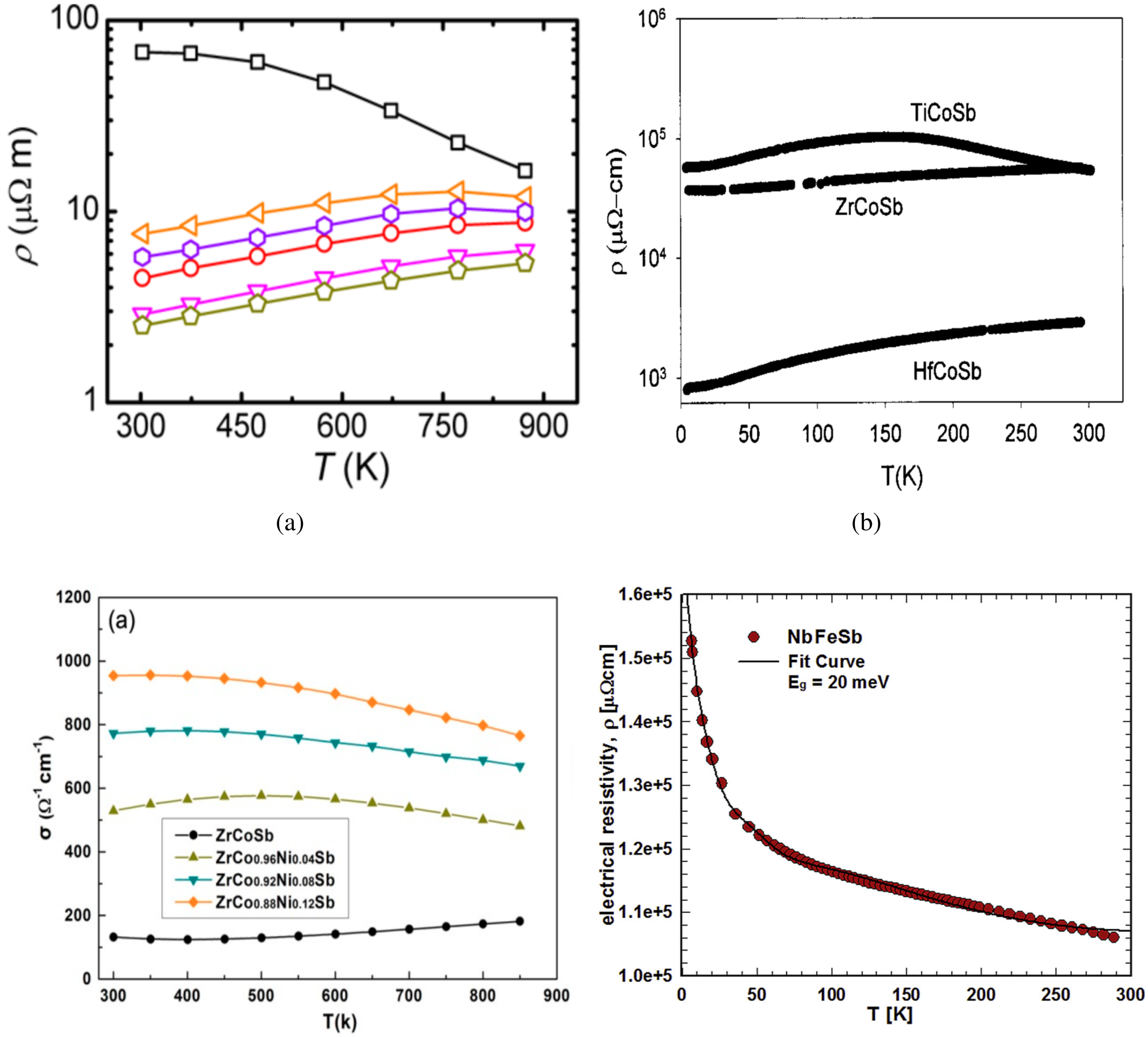

(a) (b)

(c) (d)

Figure 3.11: Resistivity of (a) ZrNiPb (black line)[18]. (b) ZrCoSb at low temperature [19]. (c) Conductivity of ZrCoSb at high temperature [20]. (d) Resistivity of NbFeSb [21]. Reprinted from [18, 19, 21] with permission. Reuse of MDPI articles requires no permission [20].

4. SUMMARY AND CONCLUSIONS

4.1 Conclusion

With the help of a low temperature high vacuum compatible interferometer, the effect of temperature on a Pan-style STM was studied and it was shown that the actual movement is more complex than the ideal expectation. By analyzing the interferometer data, we conclude that the importance of perfect alignment of the different components of the STM is paramount. With this information, the assembling process, especially the procedure of applying epoxy to glue the piezo feet to the STM body was modified. After the improvement, the STM worked reliably at liquid helium temperature.

Because STM resolves atoms and measures current of pico-amps, vibrations and electronic noise should be very low. An eddy current damper which acts as a low pass filter was implemented. Three kinds of electronic noise were carefully handled. Ground loops were alleviated by placing plugs as close as possible, gapping BNC cables, and adding plastic junctions to metal pipes. Inductive noise was reduced by turning off sources like the fluorescent lights and shielding other non-coaxial cables. Capacitive noise was reduced by using a shorter and thicker coaxial cable for the tunneling current. Because many STM experiments require scanning over a large area on the sample or locating a lithographic structure, a mechanical moving sample stage was implemented. The built stage can move the sample in steps of $1\,\mu\mathrm{m}$ with a millimeter range. The stage was also carefully designed to avoid grounding the bias voltage or propagating vibrations.

Using the STM, HfNiSn was studied. A ZBA in the STS spectra that scales as V^{α}, a variable-range hopping resistance and a 3D weak anti-localization magnetoresistance are indicative of a disordered system. Whether these properties originate from the singular lattice or intrinsic disorder is not resolved. If further study confirms the former assumption, a theory to explain the similarity between the half-Heusler structure and disordered systems is needed. If the latter is confirmed, the intrinsic disorders in these materials are not only donors but also cause localization.

4.2 Further Study

4.2.1 Half-Heusler Compounds

As mentioned in section 3.3.2, we suspect a correlation between the ZBA and the VRH resistivity. When the resistivity changes from VRH to a typical semiconductor behavior, the minima of the LDOS change from a power law to a linear temperature dependence. If the relation can be verified, we can be more certain that the two phenomena have a common origin and therefore provide an extended area for theoretical research. Some questions remain. Why temperature transfers WAL to a common semiconductor? Is it because of phonon scattering? Why the same material can have distinct crossover temperatures? The ZBA is believed to be a result of disorders and Coulomb interactions. We may need to revisit these hypotheses. Maybe the TLS proposed by J. V. Delft is correct.

It would be very interesting to obtain samples with different crossover temperatures as well as to dope HfNiSn with other elements. An alternative approach would be to purposely grow defective samples and compare them with samples after different hours of annealing. As mentioned in Section 3.3.4, different half-Heusler compounds have LDOS with different power laws and different forms of resistivity. In addition, it may be possible to understand the correlation between the two crossover temperatures by studying different half-Heusler compounds.

Another further direction would be to study the shift of the minimum of the ZBA in a magnetic field. In Section 3.3.2, we proposed two hypotheses. The first one suggests that the shift is related to the angle between the magnetic field and certain crystal orientation. To test it, we would need to vary the orientation of the sample. Alternatively, we can use a polycrystal and utilize the moving sample stage to locate grains of different orientations. The second hypothesis suggests that the shift is due to magnetic impurities. Therefore, doping the sample with some magnetic elements should affect it. If this hypothesis is supported, the role played by spin-flip scattering in these materials is another interesting topic for theorists.

REFERENCES

[1] L. Steinke, J. J. Kistner-Morris, T. F. Lovorn, H. He, A. D. Hillier, P. Miao, S. Zellman, M. Klemm, M. Green, O. Gonzalez, A. H. MacDonald, and M. C. Aronson, "Chiral transport and electronic correlations in surface states of HfNiSn single crystals," *ArXiv e-prints*, May 2018.

[2] R. Ishiguro and S. Balibar *J. Low Temp. Phys.*, vol. 140, p. 29, 2005.

[3] J. Pradhan, N. K. Das, and A. Chakraborty *Cryogenics*, vol. 57, p. 158, 2013.

[4] J. Hieulle, *Structures and Electronic Properties of Organic Self-Assembled Monolayers Characterized by STM and XPS.* PhD thesis, École Polytechnique, 09 2014.

[5] R. Coratger, J. Beauvillain, F. Ajustron, J. C. Lacaze, and C. Tremollieres *Rev. Sci. Instrum.*, vol. 62, p. 830, 1991.

[6] A. D. Kent, C. Renner, P. Niedermann, J.-G. Bosch, and O. Fischer *Ultramicroscopy*, vol. 42-44, p. 1632, 1992.

[7] `https://commons.wikimedia.org/wiki/File:Atomic_resolution_Au100.JPG`. Accessed on Jan. 25, 2019.

[8] D. Mocatta, G. Cohen, J. Schattner, O. Millo, E. Rabani, and U. Banin *Science*, vol. 332, p. 77, 2011.

[9] S. Kasiviswanathan, V. Srinivas, A. K. Kar, B. K. Mathur, and K. L. Chopra *Appl. Surf. Sci.*, vol. 115, p. 399, 1997.

[10] P. Cheng, C. L. Song, T. Zhang, Y. Y. Wang, and et al. *Phys. Rev. Lett.*, vol. 105, 2010.

[11] M. A. Reed *Materials Today*, vol. 11, 2008.

[12] T. Zhang, P. Cheng, X. Chen, J. F. Jia, and et al. *Phys. Rev. Lett.*, vol. 103, 2009.

[13] A. Kubetzka, O. Pietzsch, M. Bode, and R. Wiesandanger *Phys. Rev. B*, vol. 63, 2001.

[14] S. H. Pan, E. W. Hudson, and J. C. Davis *Rev. Sci. Instrum.*, vol. 70, p. 1459, 1999.

[15] K. Chatterjee, M. C. Boyer, W. D. Wise, and E. W. Hudson *Rev. Sci. Instrum.*, vol. 80, 2009.

[16] `https://en.wikipedia.org/wiki/Ground_loop_(electricity)`. Accessed on Feb. 1, 2019.

[17] T. F. Rosenbaum, R. F. Milligan, G. A. Thomas, P. A. Lee, T. V. Ramakrishnan, and R. N. Bhatt *Phys. Rev. Lett.*, vol. 47, p. 1758, 1981.

[18] J. Mao, J. Zhou, H. Zhu, Z. Liu, H. Zhang, R. He, G. Chen, and Z. Ren *Chem. Mater.*, vol. 29, p. 867, 2017.

[19] Y. Xia, S. Bhattacharya, V. Ponnambalam, A. L. Pope, S. J. Poon, and T. M. Tritt *J. Appl. Phys.*, vol. 88, p. 1952, 2000.

[20] D. Zhao, L. Wang, L. Bo, and D. Wu *Metals*, vol. 8, p. 61, 2018.

[21] A. Tavassoli, F. Failamani, A. Grytsiv, G. Rogl, P. Heinrich, H. Müller, E. Bauer, M. Zehetbauer, and P. Rogl *Acta Mater.*, vol. 135, p. 263, 2017.

[22] S. Lounis, "Theory of scanning tunneling microscopy," April 2014.

[23] I. P. Batra, N. García, H. Rohrer, H. Salemink, E. Stoll, and S. Ciraci *Surf. Sci.*, vol. 181, p. 126, 1987.

[24] R. J. Colton, S. M. Baker, R. J. Driscoll, M. G. Youngquist, J. D. Baldeschwieler, and W. J. Kaiser *J. Vac. Sci. Technol.*, vol. 6, p. 349, 1988.

[25] F. Ogletree and M. Salmeron *Prog. Solid St. Chem.*, vol. 20, p. 235, 1990.

[26] D. Mocatta, G. Cohen, J. Schattner, O. Millo, E. Rabani, and U. Banin *Science*, vol. 332, p. 77, 2011.

[27] F. G. Aliev, N. B. Brandt, V. V. Moshchalkov, V. V. Kozyrkov, R. V. Skolozdra, and A. I. Belogorokhov *Z. Phys. B*, vol. 75, p. 167, 1989.

[28] H.-H. Xie, J.-L. Mi, L.-P. Hu, N. Lock, M. Chirstensen, C.-G. Fu, X.-B. Z. B. B. Iversen, and T.-J. Zhu *Cryst. Eng. Comm.*, vol. 14, p. 4467, 2012.

[29] A. Berche, J. C. Tédenac, and P. Jund *Comput. Mater. Sci.*, vol. 125, p. 271, 2016.

[30] N. Mestres and J. M. Calleja *Solid State Commun.*, vol. 91, p. 779, 1994.

[31] F. G. Aliev, V. V. Kozyrkov, V. V. Moshchalkov, R. V. Scolozdra, and K. Durczewski *Z. Phys. B-Condensed Matter*, vol. 80, p. 353, 1990.

[32] A. L. Efros and B. I. Shklovskii *J. Phys. C: Solid State Phys.*, vol. 8, p. L49, 1975.

[33] A. L. Efros and M. Pollak, *Electron-Electron Interactions in Disordered Systems*. Elsevier, 1985.

[34] L. Libioulle, Y. Houbion, and J.-M. Gilles *Rev. Sci. Instrum.*, vol. 66, p. 97, 1995.

[35] K. Ahilan, M. C. Bennett, M. C. Aronson, N. E. Anderson, P. C. Canfield, E. Munoz-Sandoval, T. Gortenmulder, R. Hendrikx, and J. A. Mydosh *Phys. Rev. B*, vol. 69, p. 245116, 2004.

[36] D. Yu, C. Wang, B. L. Wehrenberg, and P. Guyot-Sionnest *Phys. Rev. Lett.*, vol. 92, 2004.

[37] B. L. Altsuler and A. G. Aronov *Solid State Commun.*, vol. 30, p. 115, 1979.

[38] W. L. McMillan *Phys. Rev. B*, vol. 24, p. 2739, 1981.

[39] J. V. Delft, D. C. Ralph, R. A. Buhrman, S. K. Upadhyay, R. N. Louie, A. W. W. Ludwig, and V. Ambegaokar *Ann. Phys.*, vol. 263, p. 1, 1998.

[40] Y. Imry and Z. Ovadyahu *Phys. Rev. Lett.*, vol. 49, p. 841, 1982.

[41] J. V. Delft, A. W. W. Ludwig, and V. Ambegaokar *Ann. Phys.*, vol. 273, p. 175, 1999.

[42] R. M. Potok, I. G. Rau, H. Shtrikman, Y. Oreg, and D. Goldhaber-Gordon *Nature*, vol. 446, p. 167, 2007.

[43] T. Cichorek, A. Sanchez, P. Gegenwart, F. Weickert, , A. Wojakowski, Z. Henkie, G. Auffermann, S. Paschen, R. Kniep, and F. Steglich *Phys. Rev. Lett.*, vol. 94, 2005.

[44] F. G. Aliev, A. I. Belogorokhov, N. Brandt, V. V. Kozyr'kov, R. V. Skolozdra, and Y. V. Stadnyk *Pis'ma Zh. Eksp. Teor. Fiz.*, vol. 47, p. 151, 1988.

[45] J. Toboła and J. Pierre *J. Alloy. Comp.*, vol. 296, p. 243, 2000.

[46] Y. Sun, C. W. Wang, L. J. Pan, X. Fu, P. H. Yin, and H. L. Zou *Carbon*, vol. 98, p. 285, 2016.

[47] A. M. Ziqan, A. F. Qasrawi, A. H. Mohammad, and N. M. Gasanly *Bull. Mater. Sci.*, vol. 38, p. 593, 2015.

[48] S. W. Cho, M. Lee, S. M. Woo, K. H. Yim, S. W. Han, W. S. Choi, and S. Y. Lee *Sci. Rep.*, vol. 8, 2018.

[49] D. V. Baxter, R. Richter, M. L. Trudeau, R. W. Cochrane, and J. O. Strom-Olsen *Journal de Physique*, vol. 50, p. 1673, 1989.

[50] A. Sahnoune, J. O. Ström-Olsen, and A. Zaluska *Phys. Rev. B*, vol. 46, 1992.

[51] M. Olivier, J. O. Strom-Olsen, and Z. Altounian *Phys. Rev. B*, vol. 33, 1986.

[52] M. L. Trudeau and R. W. Cochrane *Phys. Rev. B*, vol. 38, 1988.

[53] A. Schulte, P. Löbl, F. Küß, and E. Lüscher *J. Phys.: Condens. Matter*, vol. 4, p. 3479, 1992.

[54] B. D. Biggs, S. J. Poon, and N. R. Munirathnam *Phys. Rev. Lett.*, vol. 65, p. 2700, 1990.

[55] T.-J. Li and J. J. Lin *Phys. Rev. B*, vol. 56, 1997.

[56] P. A. Lee and T. V. Ramakrishnan *Rev. Mod. Phys.*, vol. 57, p. 287, 1985.